THESIS

MONTE CARLO DETERMINATION OF DETECTION EFFICIENCY FOR PORTAL MONITORING

Submitted by

Noah Jeffrey Blair

Department of Environmental and Radiological Health Sciences

In partial fulfillment of the requirements

For the Degree of Master of Science

Colorado State University

Fort Collins, Colorado

Spring 2024

Master's Committee:

Advisor: Alexander Brandl

Ralf Sudowe
Kimberly Jeckel

ABSTRACT

MONTE CARLO DETERMINATION OF DETECTION EFFICIENCY FOR PORTAL MONITORING

At ports of entry into the country, at high security events such as political or athletic gatherings of crowds, and at high risk locations, portal monitors are used to detect the presence of ionizing radiation and ensure radiological/nuclear materials do not fall out of regulatory control or are utilized with malicious intent. This work uses computer models to determine the probability of photon radiation being detected in polyvinyl toluene, a plastic scintillator material, for a range of source energies, truck positions relative to the detector, and cargo materials. These results are used to develop models for operators of portal monitors to predict the activity of a radioactive source given the measured count rate and integrated count measurements. A linear model of the detection efficiency produces an analytic expression of the measured count rate given the emission spectrum of a source which allows for calculation of net counts between two points on the truck's trajectory and the time derivative of the count rate. The time derivative of the count rate has a similar characteristic behavior along the truck's trajectory and has the potential to be an indicator of weak radiological sources. A MARS model allows for accurate prediction of the net count rate for truck positions and source energies not directly modeled. These models best predict detection efficiency for higher energy photons and are primarily useful for the prediction of detection of fission and activation products.

ACKNOWLEDGEMENTS

First and foremost, I would like to thank Dr. Brandl for his guidance, support, and advice on both this project and life in general. I would also like to thank Dr. Sudowe for being on my committee and providing guidance even though I was not one of his students, Dr. Jeckel for being on my committee and providing useful insight on this project, and Dr. Johnson for allowing me to think out loud at him. Additionally, Drs. Semak and Galovich from the University of Northern Colorado helped me find my passion in physics and encouraged me to continue my studies. I owe a huge debt of gratitude to Dave Oertli and Paige Witter for helping me learn to write MCNP and for running the MCNP used in this research project. I wish to thank all the current and past members of the CSU Health Physics and Radiochemistry program for their friendship and fostering a healthy environment at school.

I would also like to thank my family for all their support as I have gone on this journey. My brothers, Austyn and Ethan, and my sister, Hannah, were regular bright spots in my life through the challenges of school. My grandmothers Kathy and Karen provided regular emotional support and encouraged me to take time for myself, and my late grandfathers Ed and Bob who encouraged me to be the best version of myself. My dear friend Sean, who has been stuck with me nearly as long as my blood relatives, has been a source of joy, inspiration, and insight over the decades we have known each other.

My parents, Myrna and Jeff, fostered a love of reading and learning from a young age. Without them, I would not have had the confidence or inclination to pursue a graduate degree.

This work was funded by the United States Nuclear Regulatory Commission under grant number: 31310021M0028. Any conclusions presented are soley the responsibility of myself and does not necessarily represent the official views of the Nuclear Regulatory Commission.

DEDICATION

To my grandfather and dear friend Bo7b, whose love of learning and guidance helped me become the man I am today. I will see you on the other side.

TABLE OF CONTENTS

LIST OF TABLES

LIST OF FIGURES

Chapter 1

Introduction

1.1 Illicit Radiological and Nuclear Materials

At ports of entry into nations, high security events, and at high-risk locations, *portal monitors* are used to detect the presence of ionizing radiation. These detectors can prevent radiological and nuclear materials from falling out of regulatory control or being used for illicit purposes. Fixed radiation portal monitors (RPMs) are commonly used to monitor radiation levels within vehicles and in particular cargo trucks. Current methods utilize a *decision threshold* for the amount of radiation detected, or rate of radiation detection, when determining whether to perform a more detailed investigation of vehicles. While these methods can prevent the transportation of high activity materials, they are unable to distinguish weak or shielded sources from natural background radiation. Some developments have been made which utilize time-domain measurements of the count rate and application of Bayesian statistics to detect the weak sources. This study models the gamma radiation from a truck interior and the response of polyvinyl toluene portal monitors as a truck approaches and passes through the monitoring region.

1.1.1 Radiological Materials out of Regulatory Control

Typically, radiological materials are classified based on the potential hazards they pose. Nuclear materials broadly encompass fissionable and fissile material which can be used to induce a chain nuclear reaction. The term radiological material typically refers to radioactive materials which are commonly (though not always) fission and activation products from nuclear reactions. The term radiological material will be used to describe radiological and nuclear material in this report, and the distinction will be made when necessary. According to a 1999 International Atomic Energy Agency (IAEA) conference, the United States

Nuclear Regulatory Commission (NRC) receives at least two hundred reports of missing radiological sources a year, IAEA (1999). As noted in this report, that number likely underestimates the true number of sources which fall out of regulatory control as these are only the reported cases. Following the September 11^{th}, 2001 attacks, the IAEA commissioned a study on the radiation detection systems used at border crossings internationally at which time there were three hundred verified reports of missing radiological sources, Beck and Schmitzer (2003). These materials can range from irradiators used for research or medical applications, sources used for imaging in industrial applications, or non-radioactive material which becomes contaminated through proximity to other radioactive material.

Not all radiological material which goes missing is necessarily stolen for malicious purposes. It may be inadvertently discarded, as was the case in Goiânia, Brazil in 1988, or may be temporarily misplaced during transit, IAEA (1988). Though there is a distinction between sources which go missing, sources which are abandoned (orphaned sources), and sources which are stolen, the end goal is to locate these sources as soon as possible to minimize dose to the public and potential terrorist activity. That being said, orphaned sources and unknowingly contaminated materials are commonly found within scrap metal, while stolen sources may be located in a variety of shipments, IAEA (1999). For this reason, this study will model the detection capabilities of sources within trucks that ship both scrap metal and foodstuff.

1.1.2 Radiation Dose

Radiation describes the general process of energy in transport, regardless of medium or energy. For the purposes of this document, the term radiation will refer to particles and electromagnetic waves whose kinetic energy is sufficient to eject orbital electrons from an atom. When electrons are ionized the chemical and crystal bonds within a material are disrupted, and in some cases the electron can cause further ionization, Turner (2007).

When cells are exposed to ionizing radiation, the damage can lead to cellular death or mutations. When large amounts of energy (above approximately 100 mGy to 500 mGy) from radiation is absorbed by the body, there is the possibility for harmful tissue effects (*deterministic or non-stochastic*) in which large parts of tissues and organs are damaged potentially permanently. For smaller amounts of radiation absorbed by the body, there is an increase in cancer risk, Johnson (2017).

In 1988 Goiânia, Brazil a ^{137}Cs medical source fell out of regulatory control and was found by members of the public who thought it was just scrap metal. In the process of transporting the source to a scrap metal processing facility, the individuals received large doses of radiation and contaminated large parts of the city leading to internal doses for many members of the public. Several individuals died as a result of acute radiation syndrome and around twenty individuals had radiation burns on their skin as a result of their contact with the source. The process of treating the patients in Goiânia, responding to unexposed but concerned members of the public, and decontaminating parts of the city was a large effort on behalf of both Brazilian and international authorities, IAEA (1988).

1.1.3 Terrorism

In addition to concerns of excess dose to the public, there are concerns about the use of radiological materials in terrorist activities. The use of radiological materials in weapons can be characterized as an improvised nuclear device (IND), a radiological dispersal device (RDD), and radiation exposure device (RED), NCRP (2010), Bevelacqua (2016).

INDs utilize nuclear material and conventional explosives to induce nuclear chain reactions similar to conventional nuclear weapons. These may have a lower yield than the weapons developed by several nation states and may be unable to produce a sustained chain reaction. The INDs which do not successfully induce a fission reaction may still act as an RDD. The goal of an RDD is to spread radioactive material in an explosion thereby contaminating the region near the explosion. RDDs typically use strictly radiological material

which are commonly external and internal radiation hazards. The goal of an RED is to provide radiation dose to unsuspecting members of the public and is typically composed of gamma-emitting radiological material, NCRP (2010).

All of these methods can provide radiation dose and/or contaminate areas with radiological material which can directly harm members of the public through dose and indirectly through psychological effects. REDs and INDs are more likely to cause dose issues than RDDs, but public exposure to ionizing radiation and to radiological material can cause widespread panic which may overwhelm first responders and medical staff and may cause general anxiety.

1.1.4 Sources of Ionizing Radiation

1.1.4.1 Photon Radiation

Photons are general particles describing excitation of the electromagnetic field which mediate electric and magnetic interactions between charged particles. The energy of an individual photon is proportional to the frequency of the electromagnetic field through Planck's constant, eqn 1.1. Visible light and radio waves are examples of photons whose energy is insufficient to ionize atoms. For energies above approximately one hundred electron-volts, photons can transfer energy to orbital electrons causing them to no longer be bound to their original atom, Johnson (2017).

$$E_\gamma = h\nu \tag{1.1}$$

All photons of the same energy will interact with the same materials in identical ways. However, it is common to use different terminology for photons with different origins. High energy photons which are produced through transitions between atomic orbitals are known as x-rays. These photons are characteristic of the atom and can be used for atomic spectroscopy. Gamma-rays are analogous to x-rays for transitions between excited nuclear states. Radioactive decay and nuclear interactions commonly leave the nucleus in an excited energy

state. The nucleus may transition to a less excited nuclear state through the emission of electromagnetic radiation known as a gamma-ray. Like x-rays, gamma-rays are characteristic for the daughter nucleus in the interaction and can be used to characterize the nuclei present in a sample. Annihilation photons describe electromagnetic radiation which result from interactions of matter and anti-matter. For example, when an electron (e^-) interacts with a positron e^+, two photons with energy $E_\gamma = m_e c^2 \approx 511\,\text{keV}$ are produced, Johnson (2017).

The previous forms of electromagnetic radiation all have discrete energy spectra. However, another form of electromagnetic radiation known as bremsstrahlung radiation produces a continuous energy spectrum. When charged particles accelerate[1] some energy will be lost due to electromagnetic radiation. The energy of the individual bremsstrahlung photons will increase as the initial energy of the charged particle increases and increases with the acceleration of the particle. For electrons, this effect can be large when the electron scatters off of nuclei with a high proton content (high Z-number).

1.1.4.2 Heavy Ion Radiation

For heavy nuclei with a large proton to neutron ratio (large $Z : N$ ratio), the nucleus may decay through the emission of an alpha particle (^{4}He nucleus) or via spontaneous fission in which the nucleus splits into two smaller nuclei and several neutrons. These particles (aside from neutrons) are charged and due to their large mass have a limited range in most media, Johnson (2017). For this reason, they do not pose an external hazard, are typically shielded by their surroundings, and cannot be detected by portal monitors. The probability of a heavy ion tunnelling out of the nucleus decreases as the mass of a heavy ion increases. Due to the small mass of helium nuclei and their stability, alpha-decay requires less energy than spontaneous fission. The decay energy of alpha-emitting radionuclides typically ranges from approximately two mega-electron-volts to eight mega-electron-volts. In some cases,

[1]This includes changes in direction and speed losses.

the resulting nuclei from alpha-decay or spontaneous fission will be left in an excited state following the decay, leading to gamma-emission.

1.1.4.3 Electron Radiation

For nuclei without sufficient energy to undergo alpha-decay or spontaneous fission, or nuclei with a large neutron to proton ratio, the nucleus may undergo isobaric decay. Two nuclei are isobars if they contain the same total number of hadrons in their nucleus, $A = Z+N$. Isobaric decay is one in which A is the same for both the parent and daughter nucleus. Beta-minus decay is a form of isobaric decay which occurs in nuclei with a large neutron to proton ratio (low $Z : N$ ratio), Johnson (2017). A down quark within the neutron changes quark flavor to an up quark creating a proton, electron, and anti-electron-neutrino, eqn 1.2.

$$n \rightarrow p + e^{-} + \bar{\nu_e} \tag{1.2}$$

Since beta-minus decay is a three-body decay, the kinetic energy available is shared between the anti-neutrino and the electron leading to a continuous spectrum of electron energies. Pure-beta emitters are unstable nuclei in which the daughter nucleus is left in the ground state. For many beta-emitters, gamma-rays will be emitted following the emission of the electron. Beta-plus decay is another form of isobaric decay which occurs in nuclei with a large proton to neutron ratio (high $Z : N$ ratio) with insufficient energy to undergo alpha-decay or spontaneous fission. An up quark within a proton changes quark flavor to a down quark creating a neutron, positron, and electron-neutrino, eqn 1.3, Johnson (2017).

$$p \rightarrow n + e^{+} + \nu_e \tag{1.3}$$

Like beta-minus decay, the kinetic energy available is shared between the positron and the neutrino. Upon production and subsequent deceleration, the positron will be attracted to an electron and annihilate leading to a pair of annihilation photons with $E_\gamma \approx 511\,\mathrm{keV}$. Beta-plus decay requires the decay energy to exceed $2 \cdot m_e c^2 \approx 1.02\,\mathrm{MeV}$. If the decay

energy is insufficient for beta-plus decay, the nuclues may undergo electron-capture decay. An orbital electron from one of the inner shells combines with a proton in the nucleus to form a neutron and an electron neutrino, eqn 1.4, Johnson (2017).

$$p + e^{-} \rightarrow n + \nu_e \tag{1.4}$$

Electron capture, annihilation with a positron, and ionization will leave holes in the atomic orbitals. These holes are typically filled by outer electrons leading to the emission of x-rays. In some cases, the transition from an outer shell to the hole is *forbidden*, the difference in orbital angular momenta between the two states does not equal the spin of a photon. The transitions can still occur through x-ray emission, but the transitions are delayed. Due to the instability of the atom during this period, an electron may spontaneously drop to the hole and transfer its energy to one of the electrons from its original shell. The electron which receives the excess energy is subsequently ejected from the nucleus, Johnson (2017); this process is called Auger emission. In a similar vein, if a nuclear transition is forbidden, the energy may be transferred to an orbital electron instead of gamma emission; this process is called internal conversion.

1.1.4.4 Neutron Radiation

Neutrons, like photons, are neutral particle radiation and have a larger range in matter than electrons and heavy ions. They are commonly produced in nuclear fission reactions, and are capable of leading to *activation*, Cacuci (2010). This is the process by which a stable nucleus absorbs a neutron and becomes radioactive, typically a beta-minus emitter, Johnson (2017). Activation products along with fission products are frequent beta-gamma emitters of concern for both radiation dosimetry and potential dirty bombs. Though some portal monitors are capable of neutron detection, gamma-radiation will be the primary topic of this report.

1.1.5 Radioactive Decay Kinetics

The number of radioactive nuclei of a certain species follows first-order kinetics, eqn 1.5, Johnson (2017). The rate constant, λ, is characteristic for the radionuclide and is related to the probability of the transition from the unstable state to the stable state occurring. This kinetic law leads to exponential decay of the species present, eqn 1.6.

$$\frac{\mathrm{d}N}{\mathrm{d}t} = -\lambda N \tag{1.5}$$

$$N(t + \Delta t) = e^{-\lambda \Delta t} N(t) \tag{1.6}$$

The activity of a source is defined as the number of decays which occur in some duration, eqn 1.7. The rate constant defines a characteristic time $t = 1/\lambda$ for changes in activity of a bulk sample. Since the primary concern is nuclides which could be used for illicit purposes, this report will only consider nuclides sufficiently long-lived that the activity may be treated as a constant.

$$A(t) = \lambda N(t) \tag{1.7}$$

While activity defines the rate at which decays occur, it does not describe the rate at which photons are created. Both ^{60}Co and ^{137}Cs are common gamma-emitters in medical treatments and industrial applications, whose rate of photon production does not equal the activity. Following beta-minus decay, there is an 85.1% chance that cesium-137 will emit a 661.66 keV photon, Browne and Tuli (2006). Following beta-minus decay, there is a 99.8% chance that cobalt-60 will emit a 1173 keV photon and a 99.9% chance it will emit a 1332 keV photon, Browne and Tuli (2013). Due to these differences, the yield, $Y\left(E_{\mathrm{s}}, \Omega\right)$ is defined to be the probability density for a photon to be emitted with energy E_{s} in a direction Ω following the decay of a nuclide. The total rate of photon production in a sample of mixed nuclides is given by eqn 1.8.

$$\dot{S} = \int_{S^2} \int_0^{\infty} A \cdot Y\left(E_{\mathrm{s}}, \Omega\right) \mathrm{d}E_{\mathrm{s}} \mathrm{d}\Omega \tag{1.8}$$

For all photon processes being considered in the report, the emission is isotropic, $Y(E_{\mathrm{s}}, \Omega) = Y(E_{\mathrm{s}})/4\pi$.

1.2 Radiation Detection

The process of radiation detection in general requires the radiation to transfer or deposit energy into a detecting medium which leads to a chemical or physical response within the medium. The magnitude of this response can be associated with number of energy transfer/deposition events and/or the amount of energy transfer/deposited. Portal monitors primarily operate by counting the number of energy deposition events which occur and reporting the number of counts, n_g, or the count rate $r_g = n_g/t_g$. The subscript g indicates *gross* number of counts without correcting for background radiation. It is common practice in both laboratory and field settings to measure the number of counts in the absence of known sources of radiation to obtain a *background count rate*, r_0. The background count rate and gross count rate can be used to obtain the *net count rate*, r_n, Knoll (2010).

1.2.1 Detection Efficiency

Detection efficiency refers to both a medium's ability to respond to radiation and the ability to relate the count rate, r_n, to the rate at which radiation is produced, $\dot{S}$. The intrinsic efficiency of the detector, $\varepsilon_{\mathrm{int}}$, is the probability of a particle being registered by the detector given that it reaches the detecting medium. The absolute efficiency, $\varepsilon_{\mathrm{abs}}$ is the number of counts registered per particles generated by a radioactive source, Knoll (2010). The two types of efficiency are related by calculating the probability of a particle reaching the detecting medium as shown in Fig. 1.1. Along with the yield, the absolute efficiency can be used to relate count rate to source activity.

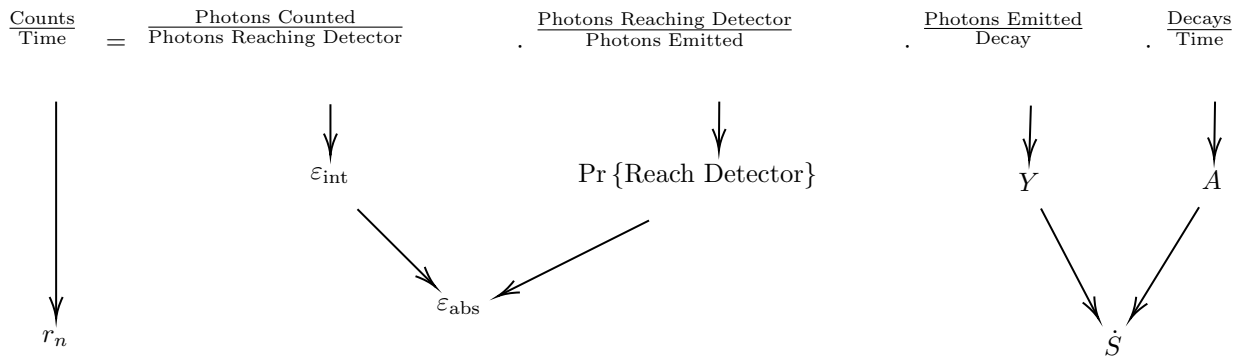

Fig. 1.1: Relationship between activity and count rate.

In laboratory settings, the absolute efficiency can be determined for a source energy using a radioactive source with known photon emission rate $\dot{S}$ and comparing the net count rate to the photon emission rate. The intrinsic efficiency can be determined by relating the count rate to the emission rate given a known probability of reaching the detector. For many counting instruments, this may be estimated by considering the solid angle of the detector as measured by the source. When shielding and complicated geometries are involved, the probability density of reaching the detector often needs to be estimated using radiation transport methods.

Another method of relating activity to the count rate is via a series of conditional probability statements for photons reaching the detector. The three primary events for photon detection are its emission with energy E_{s}, arrival at the detector with energy E_{r}, and deposition of some energy E_{d} in the detecting medium. For a simple counting experiment the probability of detection depends on the probability density of source emission at some energy, the conditional probability density of a source reaching the detector with some energy given the source energy, and the conditional probability density of energy deposition with some amount given that the photon reached the detector with some energy, eqn 1.9. This probability can be multiplied by the activity of the source to obtain the net count rate.

$$\begin{aligned}\Pr\{\mathrm{D}|\mathrm{E}\} &= \Pr\{\text{Detection}\,|\text{Emission}\} \\ &= \int_0^\infty \mathrm{d}E_\mathrm{d} \int_0^\infty \mathrm{d}E_\mathrm{r} \int_0^\infty \mathrm{d}E_\mathrm{s} \left[f_{\mathrm{D}|\mathrm{R}}\left(E_\mathrm{d}\,|E_\mathrm{r}\right) f_{\mathrm{R}|\mathrm{E}}\left(E_\mathrm{r}\,|E_\mathrm{s}\right) Y\left(E_\mathrm{s}\right) \right] \\ &= \int_0^\infty \varepsilon_\mathrm{abs}\left(E_\mathrm{s}\right) \mathrm{d}E_\mathrm{s}\end{aligned} \tag{1.9}$$

For counting instruments which do not provide spectral information, such as the plastic scintillators considered in this project, the intrinsic efficiency for a photon which reaches the detector can be expressed in terms of the distribution $f_{\mathrm{D}|\mathrm{R}}$, eqn 1.10. Similarly, the absolute efficiency can be expressed in terms of the distribution $f_{\mathrm{D}|\mathrm{E}}$, eqn 1.11.

$$\varepsilon_\mathrm{int}\left(E_\mathrm{r}\right) = \int_0^\infty f_{\mathrm{D}|\mathrm{R}}\left(E_\mathrm{d}\,|E_\mathrm{r}\right) \mathrm{d}E_\mathrm{d} \tag{1.10}$$

$$\varepsilon_\mathrm{abs}\left(E_\mathrm{s}\right) = \int_0^\infty f_{\mathrm{D}|\mathrm{E}}\left(E_\mathrm{d}\,|E_\mathrm{s}\right) \mathrm{d}E_{\gamma,\mathrm{d}} \tag{1.11}$$

1.2.2 Scintillators

Portal monitors commonly utilize a class of radiation detectors known as scintillation detectors, Ludlum Measurements (2023). When a scintillating material gets excited by ionizing radiation, it will emit optical radiation, Knoll (2010). This optical radiation can then be measured using photomultiplier tubes (PMT). There are two main types of scintillators, organic and inorganic. Organic scintillators will have characteristics that depend on the structure of the electron levels for the molecules. Because of this, there is no dependence on the physical state of the scintillating material which renders the material capable of functioning in the solid and liquid state. Inorganic scintillators operate based on the crystal structure and the associated band energies. These must remain in the solid state and depend on the type of lattice in the crystal. The polyvinyl toluene detectors used for portal monitoring are plastic (organic solid) detectors, Ludlum Measurements (2023), Rakes, Kelly D. (2008), Brooks (1979).

When a photon enters the scintillating medium, the photon will ionize an atom and the resulting electron then excites electrons within the polyvinyl toluene as it passes by them. Due to the molecular structure of organic scintillators, the electrons will de-excite through a combination of radiative (optical emission) and non-radiative transitions. The excited molecules initially will drop down to a lower energy state (but still excited) via a series of non-radiative transitions. From the lower-energy excited state, the electron may drop to the ground state emitting optical radiation (fluorescence). These transitions occur between the singlet ground state and singlet excited state. Due to similar energy levels between the excited singlet state and the excited triplet state, the molecule may undergo intersystem-crossing to an excited triplet state. When the molecule de-excites from the triplet state to the ground singlet state, optical radiation is emitted (phosphorescence). There is also the possibility of the molecule transitioning from the excited triplet state back to the excited singlet state through intersystem-crossing and de-exciting from the excited singlet state (delayed fluorescence). The ideal wave-shifting material will primarily undergo fluorescence to allow for better time correlation between events, Knoll (2010), Brooks (1979).

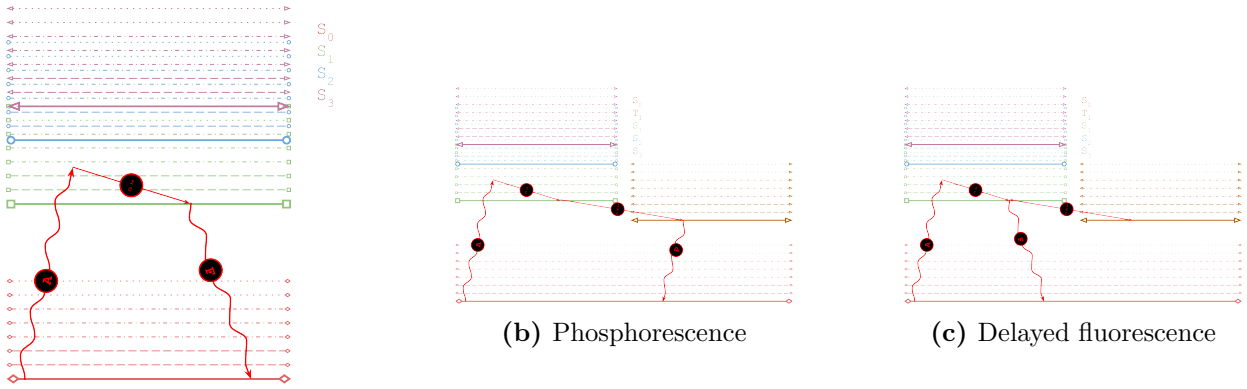

(a) Fluorescence

(b) Phosphorescence

(c) Delayed fluorescence

Fig. 1.2: Wave-shifter methods of emitting optical radiation.

When the lower energy optical photon reaches the photomultiplier tube, it interacts with a photocathode emitting a photoelectron from the surface. The electron interacts with a

series of dynodes which amplify the number of electrons passing through the tube. This electrical signal is subsequently measured as a pulse whose height is (typically) proportional to the energy deposited in the scintillator, Knoll (2010).

1.2.3 Counting Statistics

The characterization of a detector depends on the statistical fluctuations associated with radioactive decay and within the detection process. Given N identical radioactive nuclei, each will have an equal probability, π, of undergoing a nuclear transition in some time interval. The number of nuclei which undergo a transition, X, is a stochastic variable which follows a binomial distribution, $B(N, \mathfrak{p})$ with a probability mass function (pmf) given by eqn 1.12, Turner et al. (2012).

$$p_X(x) = \binom{N}{x} \cdot \mathfrak{p}^x \cdot (1-\mathfrak{p})^{N-x} \tag{1.12}$$

The mean and variance in the number of nuclei which decay are respectively given by $E\{X\} = N \cdot \mathfrak{p} = \mu$ and $\text{var}(X) = N \cdot \mathfrak{p} \cdot (1-\mathfrak{p}) = \mu \cdot (1-\mathfrak{p})$. In the case of a bulk sample the number of nuclei is typically on the order of 10^{23}, and the probability of a single atom decaying is small. Taking the limit as $N \to \infty$ and $\mathfrak{p} \to 0$ of the binomial pmf, while keeping the mean constant yields the pmf for a Poisson distribution.

$$\begin{aligned} p_X(x) &= \frac{N!}{x! \cdot (N-x)!} \cdot \left(\frac{\mu}{N}\right)^x \cdot \left(1 - \frac{\mu}{N}\right)^{N-x} \\ &\approx \frac{N^x}{x!} \cdot \frac{\mu^x}{N^x} \cdot e^{-\mu} \\ &= \frac{\mu^x e^{-\mu}}{x!} \end{aligned}$$

The Poisson distribution has a mean and variance $E\{X\} = \text{var}(X) = \mu$. As a consequence of this relationship between mean and variance, the uncertainty in the number of counts for a single counting measurement is the square root of the number of counts measured.

1.2.4 Background Radiation

When measuring a (potentially) radioactive sample, there will be measured events which are not due to radiation from the sample, typically referred to as *background* radiation. The largest source of background radiation is due to naturally occurring radioactive materials (NORM). These are typically long lived radionuclides which have been present since the formation of Earth. These include ^{40}K and nuclides present in the thorium, actinium, and uranium decay series. The amount of radiation from NORM will vary based on the geology of the surrounding area and can be affected if a truck is shipping material that has large amounts of NORM in concentrated amounts, NCRP (2009). There is also background radiation due to cosmic radiation including galactic rays and solar particles. The amount of background from cosmic radiation will depend on altitude, cloud cover, and the number of solar particles being emitted, NCRP (2009). There may also be events which are detected in the counting equipment which are due to spurious electrical signals which are amplified prior to being counted, Knoll (2010). Due to the fluctuations in background and the inherently stochastic nature of radioactive decay, the presence of counts does not necessarily indicate that radioactive material is present.

1.2.5 ISO 11929 Methodology

Several methodologies have been developed to characterize the response of ionizing radiation detectors, leading to the *characteristic limits* of detectors and detection methodologies. Characteristic limits for detectors are most commonly defined in terms of the statistics of *background* measurements. The uncertainties associated with background and source measurements allow for the decision limit, detection limit, and limits of the confidence interval to be defined, Altshuler and Pasternack (1963), Lloyd A. Currie (1968), ISO (2010). There are differences between the methodologies given including (but not limited to) confidence intervals used and notation. This overview will primarily use the notation used in ISO 11929:2010, but the other methods will be referenced when appropriate.

The decision threshold, denoted $y^{\star}$, is a value of net counts or net count rate above which a sample is determined to likely contain radiological material, ISO (2010). The decision limit is analagous to the critical level and minimum significant measured activity (MSMA) outlined by Currie and Altshuler, Lloyd A. Currie (1968), Altshuler and Pasternack (1963). The detection limit indicates performance capabilities of instruments and does not typically correspond to action thresholds when measuring a potentially radioactive sample. Similarly, the limits of the confidence interval characterize the precision in a measurement or series of measurements.

ISO 11929 formulates the estimator in the detector response (net counts, net count rate (ρ_{n}), or activity), Y, in terms of a set of parameters, $\{X_i : i \in \{1, 2, \cdots, m\}\}$, eqn 1.13. These parameters are typically the true gross count rate, $X_1 = \rho_{\mathrm{g}}$, the true background count rate, $X_2 = \rho_0$, and other calibration and correction factors based on the instrument being used, denoted as $X_{i \geq 3}$. The uncertainty in the detector response is determined through standard uncertainty propagation techniques.

$$Y = G(X_i) = (X_1 - X_2 \times X_3 - X_4) \times W(X_5, \cdots, X_m) \tag{1.13}$$

This model for the detector response is used for a one sample z-test of the net count rate, in which the null hypothesis corresponds to no radioactive material present eqn 1.14.

$$\begin{aligned} H_0 &:= \rho_n = \rho_g - \rho_0 \leq 0 \\ H_1 &:= \rho_n = \rho_g - \rho_0 > 0 \end{aligned} \tag{1.14}$$

Under the null hypothesis, the detector response is normally distributed with zero mean and with a standard deviation calculated through error propagation techniques, eqn 1.15.

$$\tilde{u}(\tilde{y} = 0) = \sqrt{W^2(x_5, \cdots, x_m) \cdot \left[(1 + x_3^2)\, u^2(r_0) + r_0^2 u^2(x_3) + u^2(x_4) \right]} \tag{1.15}$$

The decision threshold is chosen to minimize false positive events (incorrectly identifying a sample as radioactive when it is not) and is the upper limit of a confidence interval on the measured net count rate, given that the true net count rate is zero, eqn 1.16[2].

$$\begin{aligned} \Pr\left\{(-\infty, y^\star) \ni r_n \mid \rho_n = 0\right\} &= 1-\alpha \\ y^\star = \sqrt{2}\cdot \mathrm{erf}^{-1}\left(1-2\alpha\right)\cdot\sqrt{w^2\cdot\left[\left(1+x_3^2\right)u^2(r_0)+r_0^2u^2(x_3)+u^2(x_4)\right]} & \end{aligned} \tag{1.16}$$

1.3 Radiation Transport

The previous section provided an overview of sources of ionizing radiation, and in particular sources of high energy photons. The theory of radiation transport characterizes how radiation fields are distributed through media and how the fields interact with media. The fundamental equation in radiation transport is the *Boltzmann equation*, which is given in integral form in eqn 1.17. The Boltzmann equation describes the distribution of particles χ in phase space, $\mathcal{P} = \mathcal{C}\times\mathbb{R}_{\geq}\times S^2$, the set of positions (configuration space, $\mathcal{C}$), particle energies ($\mathbb{R}_{\geq}$), and directions particles may go, (S^2). The distribution of particles at some point in phase space is given by the number of particles generated at that point in phase space and the number of particles scattered into that region of phase space. The collision operator $K(\boldsymbol{P}'\rightarrow\boldsymbol{P})$ characterizes this scattering and the relevant physical interactions which occur, Kalos and Whitlock (2008).

$$\int_{\mathcal{P}}\chi(\boldsymbol{P})\mathrm{d}^6P = \int_{\mathcal{P}}S(\boldsymbol{P})\mathrm{d}^6P + \int_{\mathcal{P}}\int_{\mathcal{P}'}K\left(\boldsymbol{P}'\rightarrow\boldsymbol{P}\right)\chi(\boldsymbol{P}')\mathrm{d}^6P'\mathrm{d}^6P \tag{1.17}$$

1.3.1 Fluence and Interaction Coefficients

The primary quantities of interest obtained from the distribution function are various fluence (rate) and energy deposition (rate) functions given the source term. The particle fluence is the areal density of particles passing through a point in space, eqn 1.18, and the

[2] $\mathrm{erf}^{-1}(u)$ is the functional inverse of the error function, $\mathrm{erf}(z) = \frac{2}{\sqrt{\pi}}\int_0^z e^{-t^2}dt$.

energy fluence is the areal density of radiant energy, R, passing through a point in space, eqn 1.19, ICRU (2011).

$$\Phi(\boldsymbol{x}) = \lim_{a(\boldsymbol{x})\to 0} \frac{N(\boldsymbol{x})}{a(\boldsymbol{x})} \tag{1.18}$$

$$\Psi(\boldsymbol{x}) = \lim_{a(\boldsymbol{x})\to 0} \frac{R(\boldsymbol{x})}{a(\boldsymbol{x})} \tag{1.19}$$

The fluence rates, $\dot{\Phi} = d\Phi/dt$ and $\dot{\Psi}$, are the rates at which particles and radiant energy pass through the region of space. The energy and directional distributions of the fluence represent the fluence of particles within a certain energy range, or passing in a certain direction, ICRU (2011). The distribution of fluence rates can be used along with certain response functions to obtain quantities such as energy deposition rates, kerma, and dose, Cacuci (2010).

$$\dot{\Phi}\left(\boldsymbol{x}, E_{\gamma}\right) = \frac{\mathrm{d}\dot{\Phi}}{\mathrm{d}E_{\gamma}}$$
$$\dot{\Phi}\left(\boldsymbol{x}, \Omega\right) = \frac{\mathrm{d}\dot{\Phi}}{\mathrm{d}\Omega}$$

The cross section, σ, characterizes an effective area of a target relative to the beam which will interact with said target. There may be individual cross sections for particular events such as scattering or absorption, as well as the total cross section which characterizes the likelihood of any interaction occuring, Turner (2007).

The attenuation coefficient, eqn 1.20, is the differential probability per unit length of an interaction occurring between the photons and the target. The coefficient is the product of the total cross section and the particle density of the attenuating medium. For multiple attenuating species, the coefficient is a sum of products of the cross sections and number densities of each species present. The reciprocal of the attenuation coefficient is the mean free path, the average distance a photon travels before interacting with the medium, ICRU (2011), Kalos and Whitlock (2008)

$$\mu = \sigma \cdot N_V = -\frac{\mathrm{d} \ln N}{\mathrm{d}\ell} \tag{1.20}$$

The transfer coefficient, eqn 1.21, is the attenuation coefficient weighted by the fraction of energy the photon loses per interaction, $f\left(E_\gamma\right)$. For multiple interaction modes and species, this becomes a sum of the fraction of energy losses, cross sections, and particle densities for the different interaction modes and species. The attenuation coefficient represents the decrease in particle fluence as photons pass through the medium, and the transfer coefficient represents the decrease in the energy fluence as the photons pass through the medium, ICRU (2011).

$$\mu_{\mathrm{tr}} = f\left(E_\gamma\right) \cdot \mu = -\frac{\mathrm{d} \ln R}{\mathrm{d}\ell} \tag{1.21}$$

The absorption coefficient, eqn 1.22, is the transfer coefficient weighted by the fraction of energy transferred which is absorbed locally within the medium, $1 - g\left(E_\gamma\right)$. All three coefficients and the cross section are used to characterize the mechanisms of energy loss by photons in the attenuating medium, and how this energy loss affects the medium, ICRU (2011). These will all be encoded within the collision operator.

$$\mu_{\mathrm{en}} = \mu_{\mathrm{tr}} \cdot \left(1 - g\left(E_\gamma\right)\right) \tag{1.22}$$

1.3.2 Photon Interactions

Photons interact with matter through a variety of scattering and absorption methods depending on both the energy of the photon and the nature of the material they are traveling through. At low energies, in the optical and radiofrequency regimes, the primary interaction mechanisms are Thompson and Rayleigh scattering. The scattered photon has the same energy as the incident photon with a change in direction. For the higher energy photons resulting from nuclear interactions, these cross-sections are lower and are of less importance

than other interaction mechanisms. For photons with energies above five mega-electron-volts, the dominant interaction modes are pair-production and photo-nuclear interactions. While pair-production is possible for several energies being considered in this study, it is not the dominant interaction and is of lesser importance than photoelectric and Compton interactions, Turner (2007).

For incident photons with energies below several hundred kilo-electron-volts the dominant interaction method is the photo-electric effect. A weakly bound electron absorbs all the photon's energy and is ejected from the atom, Fig. 1.3. The kinetic energy of the resulting photoelectron is the difference between the photon's initial energy and the binding energy, eqn 1.23, Turner (2007).

$$E_{e^-} = E_\gamma - E_\mathrm{b} \tag{1.23}$$

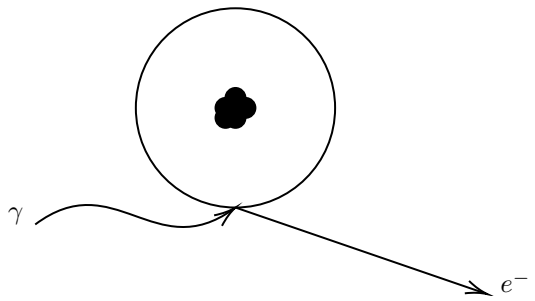

Fig. 1.3: Photoelectric effect.

For photons with energies above several hundred kilo-electron-volts and below several mega-electron-volts, the dominant interaction method is *Compton scattering*. An electron will absorb some of the photon's energy and be ejected from the atom, and the photon will be scattered at some angle off the atom with less energy, Fig. 1.4. The kinetic energy of the photon depends on the angle of scattering, eqn 1.24, and the kinetic energy of the electron is given by the difference between the energy lost by the photon and the binding energy of the electron within the atom, eqn 1.25, Turner (2007).

$$E'_\gamma = \frac{E_\gamma}{1 + \frac{E_\gamma}{m_e c^2} \cdot (1 - \cos\theta)} \tag{1.24}$$

$$E_{e^-} = E_\gamma \cdot \frac{1 - \cos\theta}{\frac{E_\gamma}{m_e c^2} + 1 - \cos\theta} - E_\mathrm{b} \tag{1.25}$$

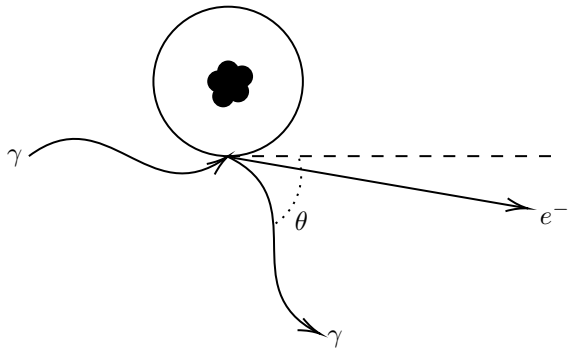

Fig. 1.4: Compton scattering.

For both of these interaction mechanisms, the energy transfer (governed by μ_tr) is the energy lost by the photon through its interaction with the electron. The ejected electrons will primarily lose energy through collisions with other electrons in the medium and through radiating bremsstrahlung. The energy lost through collisions is typically absorbed locally within the medium. The energy lost by the electron through bremsstrahlung typically is not deposited locally. For this reason, the energy absorption is governed by the absorption coefficient, μ_en. These coefficients, along with the fluence spectrum, can be used to respectively determine the energy transfer, eqn 1.26, and the energy absorbed, eqn 1.27, ICRU (2011).

$$E_\mathrm{tr} = \int_0^\infty \mathrm{d}E_\gamma \int_V \mathrm{d}V \; E_\gamma \Phi\left(\boldsymbol{x}, E_\gamma\right) \mu_\mathrm{tr}\left(\boldsymbol{x}, E_\gamma\right) \tag{1.26}$$

$$E_\mathrm{abs} = \int_0^\infty \mathrm{d}E_\gamma \int_V \mathrm{d}V \; E_\gamma \Phi\left(\boldsymbol{x}, E_\gamma\right) \mu_\mathrm{en}\left(\boldsymbol{x}, E_\gamma\right) \tag{1.27}$$

1.3.3 MCNP Transport Code

The Boltzmann Equation can be numerically integrated but is commonly solved through Monte Carlo methods. Monte Carlo integration is a statistical method of estimating integrals which samples the integrand multiple times following a defined random distribution, typically uniform. The sample mean value of these samples is an estimator for the true value of the integral. In radiation transport, Monte Carlo methods can be used to sample the distribution of source particles, model a path they travel, and compute the average value of desired quantities. These quantities, known as tallies, are often functions of the fluence and fluence distributions and can be combined with the particle emission rate to estimate quantities such as dose rate, count rate, or fluence rate. The Los Alamos Monte Carlo N-Particle transport code can perform radiation transport calculations for a variety of neutral and charged particles. This code allows for tallying on surfaces and within volumes, Table 1.1, by sampling the fluence distribution from many particle histories, Kulesza et al. (2022). These tallies can be weighted by energy, to obtain the radiant fluence from the particle fluence, and can be binned by energy to estimate distributions of quantities of interest.

Table 1.1: Common tallies used in MCNP.

Tally Type		Definition
F1	Particle Flux	$\texttt{F1} \cdot \dot{S} = \int_0^\infty \mathrm{d}E \int_{\text{Surface}} \mathrm{d}a \ \dot{\Phi}(\boldsymbol{x}, E)\boldsymbol{\Omega} \cdot \boldsymbol{n}$
$\star$ F1	Energy Flux	$\star\texttt{F1} \cdot \dot{S} = \int_0^\infty \mathrm{d}E \int_{\text{Surface}} \mathrm{d}a \ E\dot{\Phi}(\boldsymbol{x}, E)\boldsymbol{\Omega} \cdot \boldsymbol{n}$
F2	Particle Fluence Rate	$\texttt{F2} \cdot \dot{S} = \frac{1}{A_{\text{Surface}}} \int_0^\infty \mathrm{d}E \int_{\text{Surface}} \mathrm{d}a \ \dot{\Phi}(\boldsymbol{x}, E)\boldsymbol{\Omega} \cdot \boldsymbol{n}$
$\star$ F2	Energy Fluence Rate	$\star\texttt{F2} \cdot \dot{S} = \frac{1}{A_{\text{Surface}}} \int_0^\infty \mathrm{d}E \int_{\text{Surface}} \mathrm{d}a \ E\dot{\Phi}(\boldsymbol{x}, E)\boldsymbol{\Omega} \cdot \boldsymbol{n}$
F4	Particle Fluence Rate	$\texttt{F4} \cdot \dot{S} = \frac{1}{V_{\text{Cell}}} \int_0^\infty \mathrm{d}E \int_{\text{Cell}} \mathrm{d}V \ \dot{\Phi}(\boldsymbol{x}, E)\boldsymbol{\Omega} \cdot \boldsymbol{n}$
$\star$ F4	Energy Fluence Rate	$\star\texttt{F4} \cdot \dot{S} = \frac{1}{V_{\text{Cell}}} \int_0^\infty \mathrm{d}E \int_{\text{Cell}} \mathrm{d}V \ E\dot{\Phi}(\boldsymbol{x}, E)\boldsymbol{\Omega} \cdot \boldsymbol{n}$
F8	Pulse Height	$\texttt{F8} \cdot \dot{S} = \frac{1}{V_{\text{Cell}}} \int_0^\infty \mathrm{d}E \int_{\text{Cell}} \mathrm{d}V \ \dot{\Phi}(\boldsymbol{x}, E)\mu_{\text{en}}(\boldsymbol{x}, E)$
$\star$F8	Energy Deposition	$\star\texttt{F8} \cdot \dot{S} = \frac{1}{V_{\text{Cell}}} \int_0^\infty \mathrm{d}E \int_{\text{Cell}} \mathrm{d}V \ E\dot{\Phi}(\boldsymbol{x}, E)\mu_{\text{en}}(\boldsymbol{x}, E)$

1.3.4 Monte Carlo Estimation of Efficiency

The $F1$ tally along with the photon emission rate, will provide the photon flux through a surface. For the portal monitors being considered, the value of this tally at the surfaces bounding the detector will provide an estimate for the probability of a photon reaching the detector. By binning the tally by particle energy, and performing MCNP runs with multiple source energies, we can obtain a matrix which estimates the probability of a photon reaching the detector at some final energy, eqn 1.28.

$$\texttt{F1}_{ij} \approx \int_{E_{\mathrm{r},i}}^{E_{\mathrm{r},i+1}} \mathrm{d}E_{\mathrm{r}} \int_{E_{\mathrm{s},j}}^{E_{\mathrm{s},j+1}} \mathrm{d}E_{\mathrm{s}}\ f_{R|E}\left(E_{\mathrm{r}}|\, E_{\mathrm{s}}\right) \tag{1.28}$$

The $F8$ tally along with the photon emission rate, will provide rate of energy deposition events within a volume. For the portal monitors being considered, the value of this tally within the detector will provide an estimate for the probability of a photon being detected. By binning the tally by particle energy, and performing MCNP runs with multiple source energies, we can obtain a matrix which estimates the probability of a photon depositing some energy in the detector, eqn 1.28.

$$\texttt{F8}_{ij} \approx \int_{E_{\mathrm{d},i}}^{E_{\mathrm{d},i+1}} \mathrm{d}E_{\mathrm{d}} \int_{E_{\mathrm{s},j}}^{E_{\mathrm{s},j+1}} \mathrm{d}E_{\mathrm{s}}\ f_{D|E}\left(E_{\mathrm{d}}|\, E_{\mathrm{s}}\right) \tag{1.29}$$

The $F1$ and $F8$ tallies on their own are sufficient to estimate the probability of photons reaching the detector and being detected respectively. In order to obtain information about the intrinsic efficiency of a detector, we would ideally have a similar matrix whose rows correspond to energy bins of energy deposited and whose columns correspond to energy bins of photon energy at the detector, eqn 1.30.

$$Q_{ij} \approx \int_{E_{\mathrm{d},i}}^{E_{\mathrm{d},i+1}} \mathrm{d}E_{\mathrm{d}} \int_{E_{\mathrm{r},j}}^{E_{\mathrm{r},j+1}} \mathrm{d}E_{\mathrm{r}}\ f_{D|R}\left(E_{\mathrm{d}}|\, E_{\mathrm{r}}\right) \tag{1.30}$$

The matrix containing F8 tallies would then be equal to the matrix product of the matrix $\boldsymbol{Q}$ with the matrix containing the F1 tallies. The matrix containing efficiency information

can be calculated by the product of the left inverse of the F1 matrix and the F8 matrix. An estimate for the intrinsic efficiency could then be obtained by summing over all rows of this matrix, eqn 1.31[3].

$$\epsilon_{\text{int}}\left(E_{\text{r}}\right) \approx \sum_{i} \left[\mathbf{F8} \cdot \mathbf{F1}^{T} \cdot \left(\mathbf{F1} \cdot \mathbf{F1}^{T}\right)^{-1}\right]_{ij} [\![E_{\text{r}} \in \left(E_{\text{r},j}, E_{\text{r},j+1}\right)]\!] \tag{1.31}$$

[3]In this equation, $[\![P]\!]$ is the Iverson bracket which is 1 when a statement P is true and 0 when the statement is false.

Chapter 2

Methodology

2.1 Materials and MCNP Geometry

The configuration space for the Monte Carlo takes place in the following rectangular prism:

$$\mathcal{C} = \left\{ (x, y, z) \middle| \begin{array}{c} x \in [-750\,\text{cm}, 750\,\text{cm}] \wedge \\ y \in [-2500\,\text{cm}, 2500\,\text{cm}] \wedge \\ z \in [-20\,\text{cm}, 600\,\text{cm}] \end{array} \right\} \tag{2.1}$$

The lower ten centimeters of this space are made of dirt/soil, modeled using material 104 from the Pacific Northwest National Lab Compendium of Material Composition Data for Radiation Transport Modeling, Gesh et al. (2011). The next ten centimeters are composed of concrete, Gesh et al. (2011), Material 86. The rest of the configuration space will contain the portal monitors, truck, and air, Gesh et al. (2011), Material 4. A summary of the material compositions is provided in Table 2.1.

Table 2.1: General materials and mass fractions.

Material	Mass Density ($\text{g}\,\text{cm}^{-3}$)	Nuclide	Mass Fraction
Air	1.205×10^{-3}	$^{\text{nat}}$C	1.24×10^{-4}
		$^{\text{nat}}$N	7.55×10^{-1}
		$^{\text{nat}}$O	2.32×10^{-1}
		$^{\text{nat}}$Ar	1.28×10^{-2}
Concrete	1.032	$^{\text{nat}}$H	4.53×10^{-3}
		$^{\text{nat}}$O	5.13×10^{-1}
		$^{\text{nat}}$Na	1.53×10^{-2}

Material	Mass Density ($\mathrm{g\,cm^{-3}}$)	Nuclide	Mass Fraction
Earth	1.520	$^{\mathrm{nat}}\mathrm{Al}$	3.56×10^{-2}
		$^{\mathrm{nat}}\mathrm{Si}$	3.60×10^{-1}
		$^{\mathrm{nat}}\mathrm{Ca}$	5.79×10^{-2}
		$^{\mathrm{nat}}\mathrm{Fe}$	1.38×10^{-2}
		$^{\mathrm{nat}}\mathrm{H}$	2.38×10^{-2}
		$^{\mathrm{nat}}\mathrm{O}$	5.99×10^{-1}
		$^{\mathrm{nat}}\mathrm{Al}$	8.04×10^{-2}
		$^{\mathrm{nat}}\mathrm{Si}$	2.97×10^{-1}

2.1.1 Portal Monitor

The portal monitors used are based on generic versions of Ludlum Model 4525 detectors. The detecting medium is composed of PVT, Gesh et al. (2011), Material 256. The generic version of the monitor being used has a height of 156 cm, a width of 152 cm, and a depth of 8.8 cm, Ludlum Measurements (2023). This thickness is sufficient for an interaction to be likely within the detector for most photon energies of interest, Fig. 2.2. The PVT is surrounded by 0.64 cm of lead on all sides except for the side closest to the truck to reduce background signal. The PVT and lead are held in a three centimeter thick carbon steel container, Gesh et al. (2011), Material 294. The two portal monitors are separated by 359 cm, a common configuration for Ludlum portal monitors, Ludlum Measurements, Inc. (2022). A summary of these materials used is located in Table 2.2.

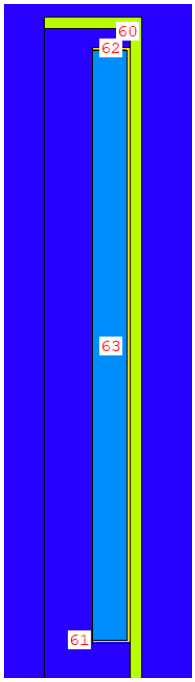

Fig. 2.1: Configuration of portal monitor used for radiation transport.

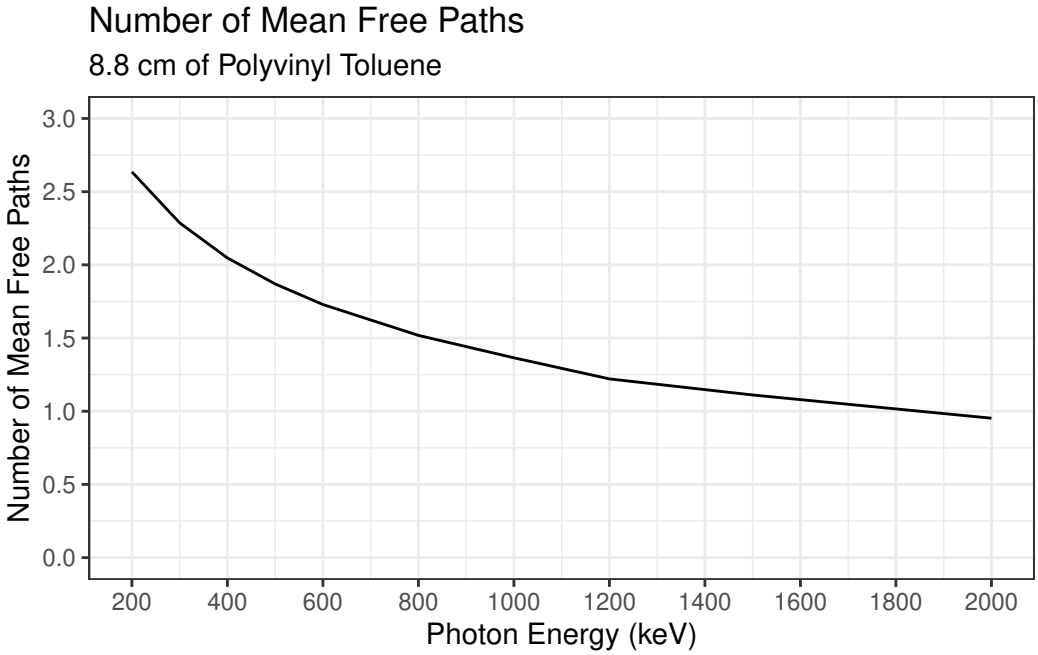

Fig. 2.2: Number of mean free paths photons of various energies will travel through the thickness of the portal monitor. Data taken from the radiological health handbook, Johnson and Birky (2012).

Table 2.2: Materials and mass fractions for portal monitors.

Material	Mass Density ($\mathrm{g\,cm^{-3}}$)	Nuclide	Mass Fraction
Polyvinyl	2.250	$^{\mathrm{nat}}$H	8.50×10^{-2}
Toluene		$^{\mathrm{nat}}$C	9.15×10^{-1}
Carbon Steel	7.820	$^{\mathrm{nat}}$C	5.00×10^{-3}
		$^{\mathrm{nat}}$Fe	9.95×10^{-1}
Lead	11.350	$^{\mathrm{nat}}$Pb	1.00

2.1.2 Truck Trailer

The exterior of the truck was modeled after the *Strick Elevator*™. The exterior dimensions of the truck are 8.53 m × 2.60 m × 2.81 m and the bottom of the truck is 1.3 m off the ground. The bottom of the truck is 3.5 cm thick, the sides are 0.122 cm thick, and the roof is 0.122 cm thick, Strick Trailers (2021). Trailers commonly have thicker regions surrounding the walls to provide structural supports. These compose a small fraction of the surface area of the truck and have not been included in the model of the truck. The truck itself is assumed to be composed of pure aluminium, Gesh et al. (2011), Material 6, without any composite materials present, Table 2.3. These assumptions may increase the likelihood of photons reaching the detector.

The materials composing the truck interior will depend on the cargo being transported. This study considers transport of scrap metal and the transport of foodstuff. The usable volume for the truck is 59.25 $\mathrm{m^3}$, Strick Trailers (2021). Due to both regulatory and engineering constraints, this entire volume cannot be filled with scrap metal, (modeled using Gesh et al. (2011), Material 296). The United States Federal Highway Administration limits the total mass of vehicles, cargo, and trailers at 36.3 Mg (8×10^4 lb)[4], Federal Highway Administration (2016). Even if the total usable volume were legally allowed to be filled with scrap metal,

[4] 1 Mg = 10^6 g

the flatbed trailer would be unable to support this mass. A 2016 study by Panganiban et al. analyzed optimization methods to decrease trailer mass while maintaining the same mass carrying capacity. Their model allows a cargo mass of 20 Mg which is consistent with US regulations, Panganiban et al. (2016). Using this mass as the total mass allowed in the truck, the metal will take up 4.29% of volume, 99.66% of the mass, and the interior will have a total density of $0.339\,\mathrm{g\,cm^{-3}}$. A summary of mass fractions and density for the scrap metal interior is presented in Table 2.3.

For transport of foodstuff the interior was modeled using ICRP soft tissue, Gesh et al. (2011) Material 320, ICRP (2003). The elements found when modeling soft tissue are consistent with atomic spectroscopy measurements performed on food, and the amount of trace materials present in food which are not present in ICRP soft tissue are in low enough mass fractions to be negligible, Patriarca et al. (2021). The use of ICRP tissue most closely models the transport of meat and may not be a good surrogate for transport of vegetables and grain. The volume fraction of foodstuff cargo varies depending on the specifics of the cargo, whether refrigeration is required, and the distance being traveled. These effects are covered in a study performed by Wang et al. which found packing efficiency (volume fractions of cargo) ranging from 30% to 90%, Wang et al. (2019). The effects of packing efficiency on trucks carrying foodstuff will be discussed later. For the time being, a packing efficiency of 50% will be used for the majority of the analysis. Using this volume fraction of food, the mass fraction of the food is 99.88%, and the bulk density is $0.501\,\mathrm{g\,cm^{-3}}$. A summary of mass fractions and density for the scrap metal interior are in Table 2.3.

The materials used to model the cargo in the truck are uniform in density for each element present, without any further structure. In reality, there will be regions which contain cargo and regions which contain air. Adding this structure will increase computation time and may not have a drastic impact on the radiation which reaches the exterior of the truck. When considering the areal density of electrons with which a photon may interact with inside the truck, there is minimal difference between discrete regions and a continuous material. In

particular, for scrap metal, the bent structure of the metal when it is being transported leads to regions of air and metal which are localized together. If the energy deposition within the truck were of interest, this added structure would be needed. The placement of the truck relative to the portal monitors and ground is shown in Fig. 2.3.

Table 2.3: Materials and mass fractions for truck and contents.

Material	Mass Density ($\mathrm{g\,cm^{-3}}$)	Nuclide	Mass Fraction
Aluminium	2.699	$^{\mathrm{nat}}$Al	1.00
Foodstuff	$5.006 \cdot 10^{-1}$	$^{\mathrm{nat}}$H	1.04×10^{-1}
		$^{\mathrm{nat}}$C	2.31×10^{-1}
		$^{\mathrm{nat}}$N	2.57×10^{-2}
		$^{\mathrm{nat}}$O	6.30×10^{-1}
		$^{\mathrm{nat}}$Na	1.13×10^{-3}
		$^{\mathrm{nat}}$Mg	1.30×10^{-4}
		$^{\mathrm{nat}}$P	1.33×10^{-3}
		$^{\mathrm{nat}}$S	1.99×10^{-3}
		$^{\mathrm{nat}}$Cl	1.34×10^{-3}
		$^{\mathrm{nat}}$Ar	1.54×10^{-5}
		$^{\mathrm{nat}}$K	1.99×10^{-3}
		$^{\mathrm{nat}}$Ca	2.30×10^{-4}
		$^{\mathrm{nat}}$Fe	4.99×10^{-5}
		$^{\mathrm{nat}}$Zn	3.00×10^{-5}
Scrap	3.387×10^{-1}	$^{\mathrm{nat}}$C	7.48×10^{-4}
Metal		$^{\mathrm{nat}}$N	3.82×10^{-2}
		$^{\mathrm{nat}}$O	7.89×10^{-4}
		$^{\mathrm{nat}}$Si	4.98×10^{-3}
		$^{\mathrm{nat}}$P	2.99×10^{-3}

Material	Mass Density ($\mathrm{g\,cm^{-3}}$)	Nuclide	Mass Fraction
		$^{\mathrm{nat}}$S	1.49×10^{-4}
		$^{\mathrm{nat}}$Ar	4.67×10^{-5}
		$^{\mathrm{nat}}$Cr	1.79×10^{-1}
		$^{\mathrm{nat}}$Mn	8.72×10^{-2}
		$^{\mathrm{nat}}$Fe	6.73×10^{-1}
		$^{\mathrm{nat}}$Ni	4.98×10^{-2}

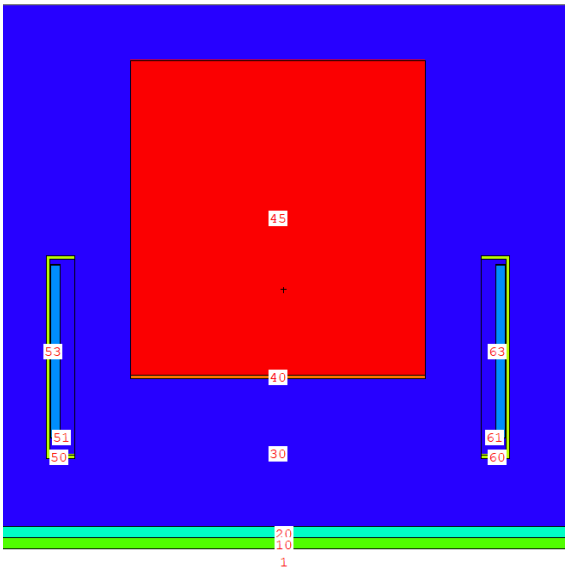

Fig. 2.3: Geometry of truck with portal monitors.

2.2 Truck Position and Source Energy

The photon source is located at the center of the truck and is modeled as a point source. Using a point source neglects effects of self-attenuation which may be important for large dense sources. Additionally, this does not account for potential intentional shielding which may be present for sources which are smuggled. This shielding can be accounted for by analyzing the spectrum of photons which exit the shield and using this spectrum as an

emission source. For a point source, the fluence is proportional to $1/r^2$ in which r is the distance to the source. For extended sources, the fluence will contain terms proportional to higher powers of $1/r$ which are more important for closer distances. For sufficiently far distances from an extended source, the dominant term will be $1/r^2$, Johnson (2017).

The different MCNP runs are parameterized by y, the component of the displacement from the center of the truck to the center of the portal monitors. At $y = 0\,\text{cm}$, the center of the truck is aligned with the portal monitors, and at $y = -250\,\text{cm}$, the truck is displaced along the y-axis Fig. 2.4. The set of positions, given in eqn 2.2, will model the truck and source relative to the detectors when the truck is approaching the portal monitors. These different positions will not model the effect of the truck position relative to the detectors on their measured background radiation. As the truck passes over the ground near the monitors, the photons from NORM within the ground may be shielded by the truck temporarily decreasing the level of background radiation, Lo Presti et al. (2006). Since the only sources considered in this study are sources within the truck, this effect will not show up within the model.

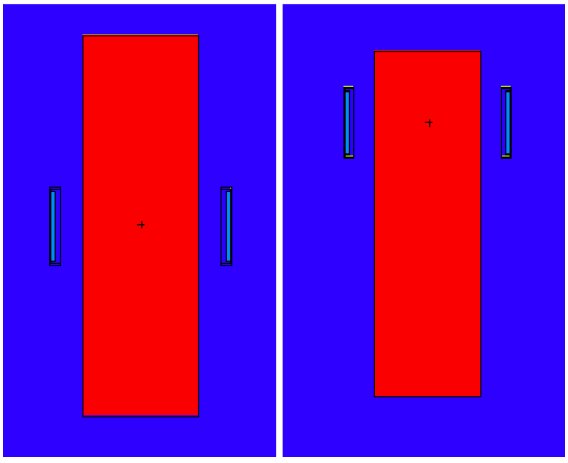

Fig. 2.4: Top down view of truck when $y = 0\,\text{cm}$ (left) and when $y = -250\,\text{cm}$ (right).

$$y \in \left\{ \begin{array}{c} 0\,\text{cm}, -250\,\text{cm}, -500\,\text{cm}, -750\,\text{cm}, \\ -1000\,\text{cm}, -1250\,\text{cm}, -1500\,\text{cm} \end{array} \right\} \tag{2.2}$$

The gamma rays associated with radioactive decay have energies which typically range from about 1 keV to about 2 MeV, Firestone (1999). For photons whose energy is between 1 keV and around 250 keV, the attenuation coefficients are significant enough that there is a low probability of these photons escaping the truck. For this reason, the source energy for the various MCNP inputs varied from 200 keV to 2 MeV in 50 keV increments. Only using data down to 200 keV does neglect gamma rays which can be emitted by types of nuclear material. The low energy and low yield of these gamma rays does indicate that these sources are unlikely to be detected in the scenarios being considered in this report.

In addition to these energies, the energy from photons following the decay of ^{137}Cs, ^{60}Co, and electron annihilation energies were included, eqn 2.3, Browne and Tuli (2006), Browne and Tuli (2013).

$$E_{\gamma,\text{s}} \in \left\{ \begin{array}{c} 200\,\text{keV}, 250\,\text{keV}, 300\,\text{keV}, 350\,\text{keV}, 400\,\text{keV}, \\ 450\,\text{keV}, 500\,\text{keV}, 511\,\text{keV}, 550\,\text{keV}, 600\,\text{keV}, 650\,\text{keV}, \\ 661.6\,\text{keV}, 700\,\text{keV}, 750\,\text{keV}, 800\,\text{keV}, 850\,\text{keV}, 900\,\text{keV}, \\ 950\,\text{keV}, 1000\,\text{keV}, 1050\,\text{keV}, 1100\,\text{keV}, 1150\,\text{keV}, \\ 1173\,\text{keV}, 1200\,\text{keV}, 1250\,\text{keV}, 1300\,\text{keV}, 1332\,\text{keV}, 1350\,\text{keV}, \\ 1400\,\text{keV}, 1450\,\text{keV}, 1500\,\text{keV}, 1550\,\text{keV}, 1600\,\text{keV}, 1650\,\text{keV}, \\ 1700\,\text{keV}, 1750\,\text{keV}, 1800\,\text{keV}, 1850\,\text{keV}, 1900\,\text{keV}, 1950\,\text{keV}, 2000\,\text{keV} \end{array} \right\} \tag{2.3}$$

2.3 MCNP Tallies

For each portal monitors surface that is closest to the truck F1 (particle flux) and F2 (particle fluence) tallies will be tracked, and within each portal monitoring volume the F4 (particle fluence) and F8 (pulse height) tallies will be tracked. Additionally, the correspond-

ing energy weighted tallies will be tracked. Each tally will be binned in 10 keV increments from 0 MeV to 2 MeV. While the fluence tallies and energy weighted tallies are not required for estimation of the probabilities of detection, they provide useful information characterizing the distribution of photons in space that may be useful for future studies.

2.4 Variance Reduction

MCNP performs several statistical checks on each tally to ensure the precision and accuracy of the results. The primary numerical checks are on the relative uncertainty, eqn 2.4, and the variance of the variance of a tally, eqn 2.5. The relative uncertainty is a measure of the precision of a tally, and includes the likelihood of a tally being scored and the variations within events which to score. The variance of the variance measures the relative precision of the relative uncertainty as an estimator for the true relative uncertainty in the tally. For the tallies being used for this analysis, both the relative uncertainty and variance of the variance should be below 10%, Kulesza et al. (2022).

$$\mathrm{u_{rel}}\left(\bar{x}\right) = \frac{u\left(\bar{x}\right)}{\bar{x}} = \frac{\sqrt{\langle x^2\rangle - \langle x\rangle^2}}{\sqrt{N}\cdot\langle x\rangle} \propto \frac{1}{\sqrt{N}} \tag{2.4}$$

$$\mathrm{VOV}\left(\bar{x}\right) = \frac{\hat{\sigma}^2\left(\hat{\sigma}^2\left(\bar{x}\right)\right)}{\hat{\sigma}^2\left(\bar{x}\right)} = \frac{1}{N}\left[\frac{\left\langle\left(x-\bar{x}\right)^4\right\rangle}{\left\langle\left(x-\bar{x}\right)^2\right\rangle^2} - 1\right] \propto \frac{1}{N} \tag{2.5}$$

To ensure these conditions were met, several preliminary MCNP runs were performed using 10^8 particle histories to determine the number of histories required for both the relative error and variance of the variance, Fig. 2.5.

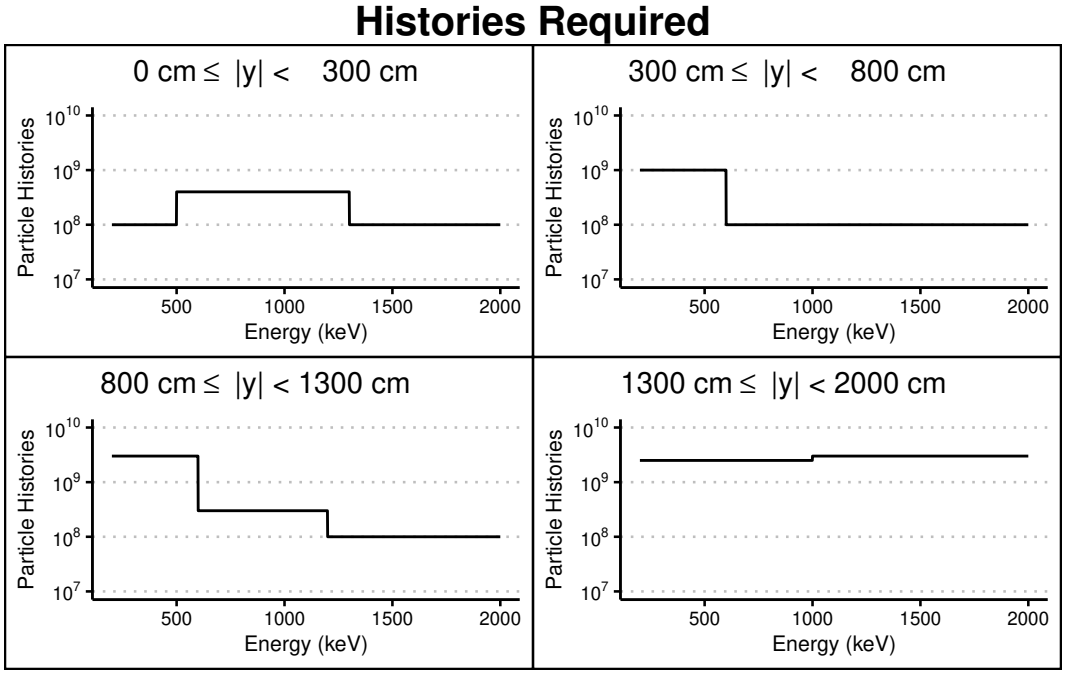

Fig. 2.5: Particle histories required for different source energies and truck positions.

In addition to increasing particle history number for different runs, configuration space had varying *importance* for different regions and starting particles. When each particle is generated, it has a weight which is used when calculating the value of a tally at the end of the run. It is possible to bias the source to emit in certain directions by increasing the number of particles emitted towards the detector, but providing these particles with a lower starting weight. This method decreases the component of the uncertainty associated with the number of particles which score in a tally region. For these runs source biasing was not used, though it may be used for future applications.

Everywhere within the configuration space described in eqn 2.1 has been assigned an equal weight except for in the soil. The soil has half the importance of the rest of the space causing half the photons which enter this region to be terminated immediately, while the other half had their weight doubled. Given the low likelihood of photons traveling through the truck, air, and concrete only to scatter within the soil to reach the detector, this method reduces computation time on photons which are unlikely to be detected.

The region outside the space described in eqn 2.1 has an importance of zero. Any photons which reach this bounding region will be immediately terminated and the next history will begin. Again, the likelihood of photons being scattering off air at these points or traveling through the soil and scattering and reaching the detector is deemed negligibly small.

2.5 Input Generation and Output Processing

The various MCNP input files were generated using the R Statistical Programming language, and several packages for statistical and numerical methods R Core Team (2023), Wickham et al. (2019), Oehlschlägel and Silvestri (2020), Borchers (2022). R along with these packages was used to parse the MCNP output files and analyze the data.

Chapter 3

Results

The primary results of importance are the probability of photons reaching the detector and their probability of detection. As expected, the distance of the truck from the detector is a major contributor to the likelihood of detection and reaching the portal monitor. For truck distances greater than 500 cm, the probability of detection and reaching the portal monitor decreases rapidly for increasing distances. The energy of source photon is another major contributor for the likelihood of reaching the detector and for detection. For low energies, the likelihood of photoelectric scattering in the cargo or truck is high enough that many photons will not reach the detector. These effects for low energy sources will not account for lower energy gamma rays and low emission yields which occur for many nuclear materials. As the initial energy increases, the probability of reaching the detector appears to asymptotically approach a fixed value for a particular position and cargo type. Once the photons have sufficient energy to reliably exit the truck, the primary factor affecting reaching the detector is whether their path will intersect with the portal monitor. Finally, there are notably differences between the foodstuff cargo and the scrap metal cargo due to their different attenuation coefficients at different energies.

3.1 Statistical Checks

From the statistical checks provided by MCNP, the relative error and variance of the variance were less than 10% for all truck and source configurations except for when the source energy was 140 keV. This is the lowest source energy considered and is unlikely to reach the detector and be detected at nearly all distances. Therefore, the component of the uncertainty associated with the likelihood of a score being achieved will be very high. At source energies below 200 keV, the large uncertainties must be taken into consideration and the results may be questionable.

The other statistical checks of note were the behavior of the mean and the distribution of tallies (the pdf-slope). Ideally, the mean behavior should be constant or fluctuating about a value during the last half of the histories run, and the distribution of events should be localized near the mean. For scenarios in which the truck was at a distance of 10 m or more from the detection region, the mean behavior often followed a monotonic behavior and did not have a distribution localized about the mean. This likely reflects the fact that a small fraction of particles reached the detector, Fig. 3.3. While there were a sufficient number of particle histories to minimize the relative error in the results, there is still a large enough variability in the number of particles which score. This leads to the distribution, and its evolution through the problem, not satisfying the requirements that MCNP typically requires for its results. Given that there is an expectation of few particles reaching the detector, this on its own does not invalidate the qualitative results, though the uncertainties must be kept in mind for the exact values of the quantitative results. Further studies which seek to obtain more accurate data will utilize more of the variance reduction techniques discussed earlier.

3.2 Energy Weighting and Parity Differences

Given all the events being tracked throughout all MCNP runs and histories, there is a level of redundancy. Both particle-based tallies and energy weighted tallies were tracked, and all tallies are tracked in both monitors which are symmetric about the source. To determine the useful information present in the energy weighted tallies, the relative difference was computed for each energy bin between the energy tally and the particle tally multiplied by the energy of the bin, eqn 3.1. The distribution of the relative differences can be seen in Fig. 3.1.

$$\text{Relative Difference} = \frac{\text{Tally}_{\text{Energy}} - E_{\text{bin}} \cdot \text{Tally}_{\text{Particle}}}{\frac{1}{2}\left(\text{Tally}_{\text{Energy}} + E_{\text{bin}} \cdot \text{Tally}_{\text{Particle}}\right)} \tag{3.1}$$

The distribution indicates that multiplying each binned tally by the energy of said bin will overestimate the purely energy weighted quantities. This is because the energy of the bin represents the upper bound of particle energies for the bin. Therefore, any calculations of radiant energy quantities (flux, fluence, etc) that utilize information from the particle tallies will overestimate. With this in mind, the majority of the calculations will utilize the particle tallies.

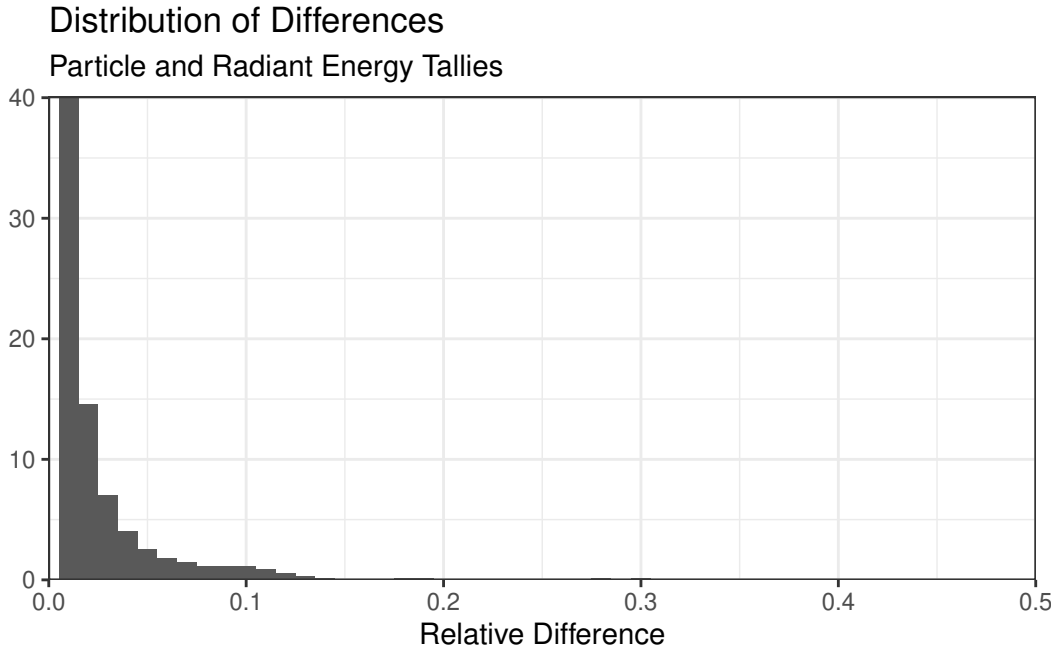

Fig. 3.1: Distribution of differences between particle tallies and radiant energy tallies.

To determine the useful information present in the tallies performed on the left portal monitor versus the right monitor (parity differences), the relative difference was calculated for each tally, eqn 3.2. The distribution of the relative differences can be seen in Fig. 3.2.

$$\text{Relative Difference} = \frac{\text{Tally}_{\text{Left}} - \text{Tally}_{\text{Right}}}{\frac{1}{2}\left(\text{Tally}_{\text{Left}} + \text{Tally}_{\text{Right}}\right)} \tag{3.2}$$

This distribution is symmetric which indicates that the average between the left and right tally is a good representative of the value for a score on either one. The distribution of parity differences does include several tallies which have a relative difference greater than

one. The variability between these tallies will be captured when calculating the uncertainty of the mean tally value.

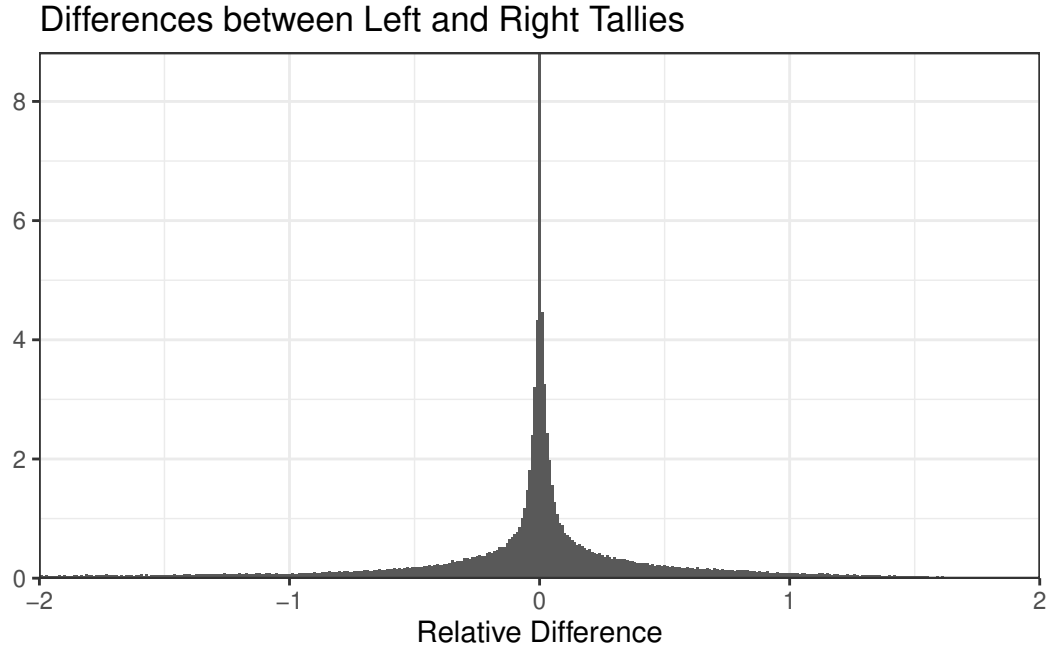

Fig. 3.2: Distribution of differences between tallies on left RPM and right RPM.

3.3 Probability of Reaching Detector

The probability of a photon reaching a detector given its emission is given by the F1 tally from the MCNP results. Using the matrix defined in eqn 1.28, the probability of the photon reaching the detector with any final energy, given its initial energy and position, is described by eqn 3.3.

$$\begin{aligned} p_{\mathrm{R}}\left(E_{\mathrm{s}}, y\right) &= \Pr\left\{\mathrm{R}\,|\mathrm{E}; E_{\mathrm{s}}, y\right\} \\ &= \int_0^{\infty} f_{\mathrm{R|E}}\left(E_{\mathrm{r}}\,|E_{\mathrm{s}}; y\right) \mathrm{d}E_{\mathrm{r}} \\ &\approx \frac{1}{2} \sum_i \left(\mathtt{F1}_{ij}^{\mathrm{left}}(y) + \mathtt{F1}_{ij}^{\mathrm{right}}(y)\right) \left[\!\left[E_{\mathrm{s}} \in \left(E_{\mathrm{s},j}, E_{\mathrm{s},j+1}\right)\right]\!\right] \end{aligned} \tag{3.3}$$

As seen in Fig. 3.3, the probability of a photon reaching a detector decreases rapidly as the truck's distance from the monitors increases. Additionally, photons whose source energy

is below five-hundred kilo-electron-volts are significantly less likely to reach the detector than those with higher energies. The low likelihood of detection for low energy photon emitters is problematic for various nuclear materials which have low energy gamma emissions whose yield is small. As the energy of the photons increases, the probability of a photon reaching the detector asymptotically approaches an energy independent value. This is likely due to the fact that these photons have similar probabilities of exiting the truck.

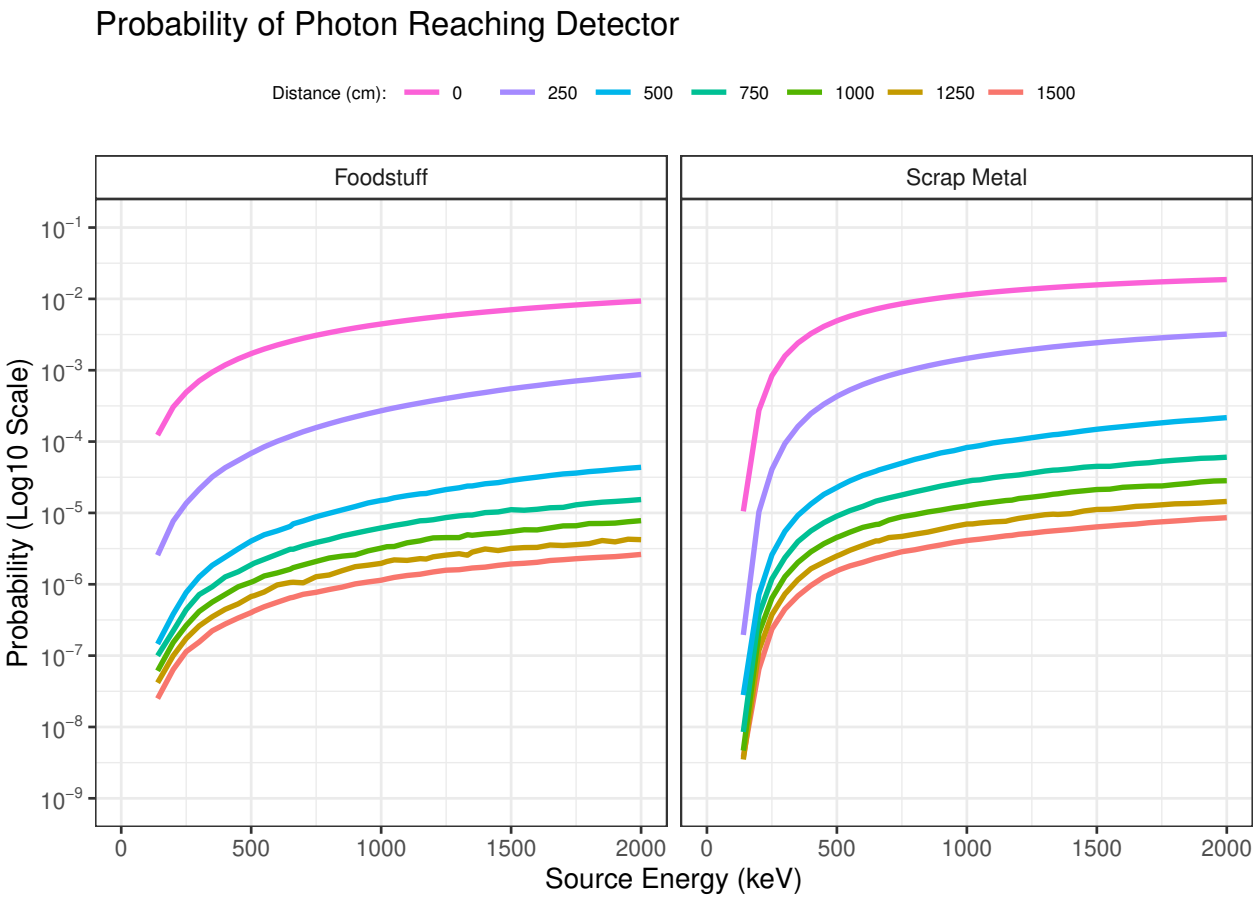

Fig. 3.3: Probability of photon reaching detector from truck for different cargo types and distances.

For higher energy photons, the probability of reaching the truck is larger when the cargo is scrap metal compared to foodstuff. For lower energy photons, this probability drops off in the truck carrying scrap metal compared to the truck carrying food stuff. This can be explained by the total attenuation coefficient of the scrap metal cargo compared to the

foodstuff cargo, Fig. 3.4. For energies below one hundred kilo-electron-volts, the attenuation coefficient is higher for scrap metal cargo. At lower energies, the dominant interaction mechanism is photoelectric absorption which is highly dependent on the presence of high-Z materials. These materials are found more in scrap-metal than foodstuff. Above one hundred kilo-electron-volts, the attenuation coefficient is higher for foodstuff cargo. At these energy ranges, the dominant interaction method is Compton scatter which is less dependent on the presence of high-Z materials. However, the average density of the foodstuff cargo is higher than the average density of the scrap metal cargo. For foodstuff cargo with lower packing efficiency, the likelihood of reaching the detector will likely be higher than scrap metal for all energies.

For all of the source photon energies, the mean free path in both materials ranges from ten centimeters to one meter. Therefore, there is a high probability of an interaction occurring within the truck. If a lower energy source photon is scattered within the truck, the resulting energy may be below one hundred kilo-electron-volts where further interactions are more likely within the scrap metal truck.

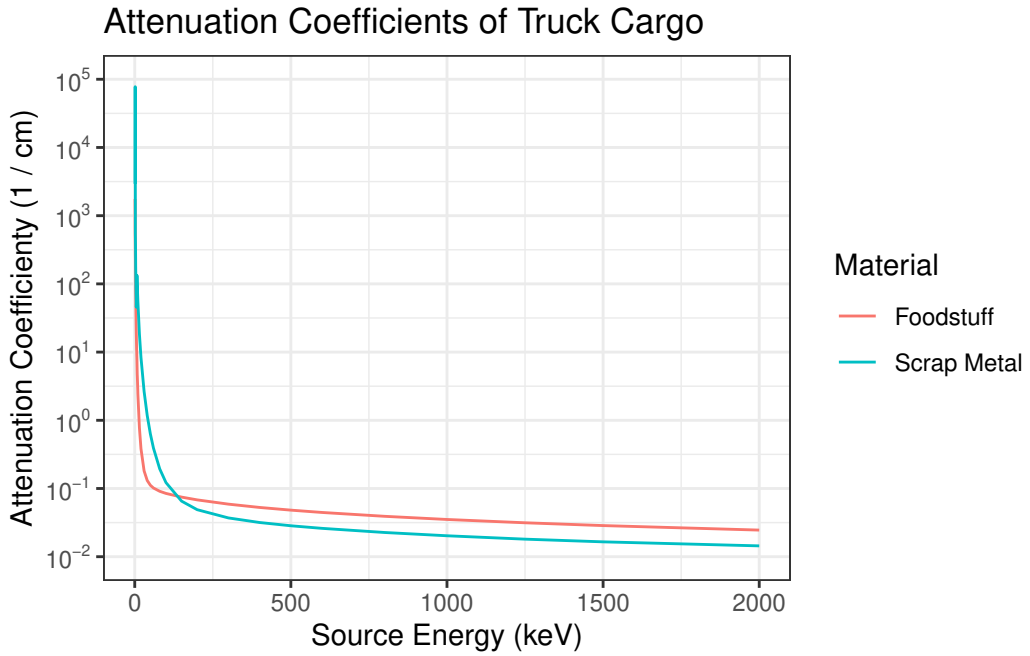

Fig. 3.4: Attenuation coefficients of scrap metal cargo and foodstuff cargo. Data taken from radiological health handbook, Johnson and Birky (2012).

3.4 Probability of Detection

The probability of a photon being detected given its emission is given by the F8 tally from MCNP results. Using a similar procedure for the probability of a photon reaching the detector, the probability of detection, can be written using the matrix defined in eqn 1.29, which is presented by eqn 3.4.

$$\begin{aligned} p_{\mathrm{D}}\left(E_{\mathrm{s}}, y\right) &= \Pr\left\{\mathrm{D}\,|\mathrm{E}; E_{\mathrm{s}}, y\right\} \\ &= \int_0^{\infty} f_{\mathrm{D}|\mathrm{E}}\left(E_{\mathrm{d}}\,|E_{\mathrm{s}}; y\right) \mathrm{d}E_{\mathrm{d}} \\ &\approx \frac{1}{2} \sum_i \left(\mathtt{F8}_{ij}^{\mathrm{left}}(y) + \mathtt{F8}_{ij}^{\mathrm{right}}(y)\right) \left[\!\left[E_{\mathrm{s}} \in \left(E_{\mathrm{s},j}, E_{\mathrm{s},j+1}\right)\right]\!\right] \end{aligned} \tag{3.4}$$

The measured detection probabilities for various truck positions and cargo materials is given in Fig. 3.5. Many of the qualitative behaviors of these curves are similar to the probability of reaching the detector. Most of the factors which determine whether or not a photon is detected are determined by whether the photon reaches the detection medium.

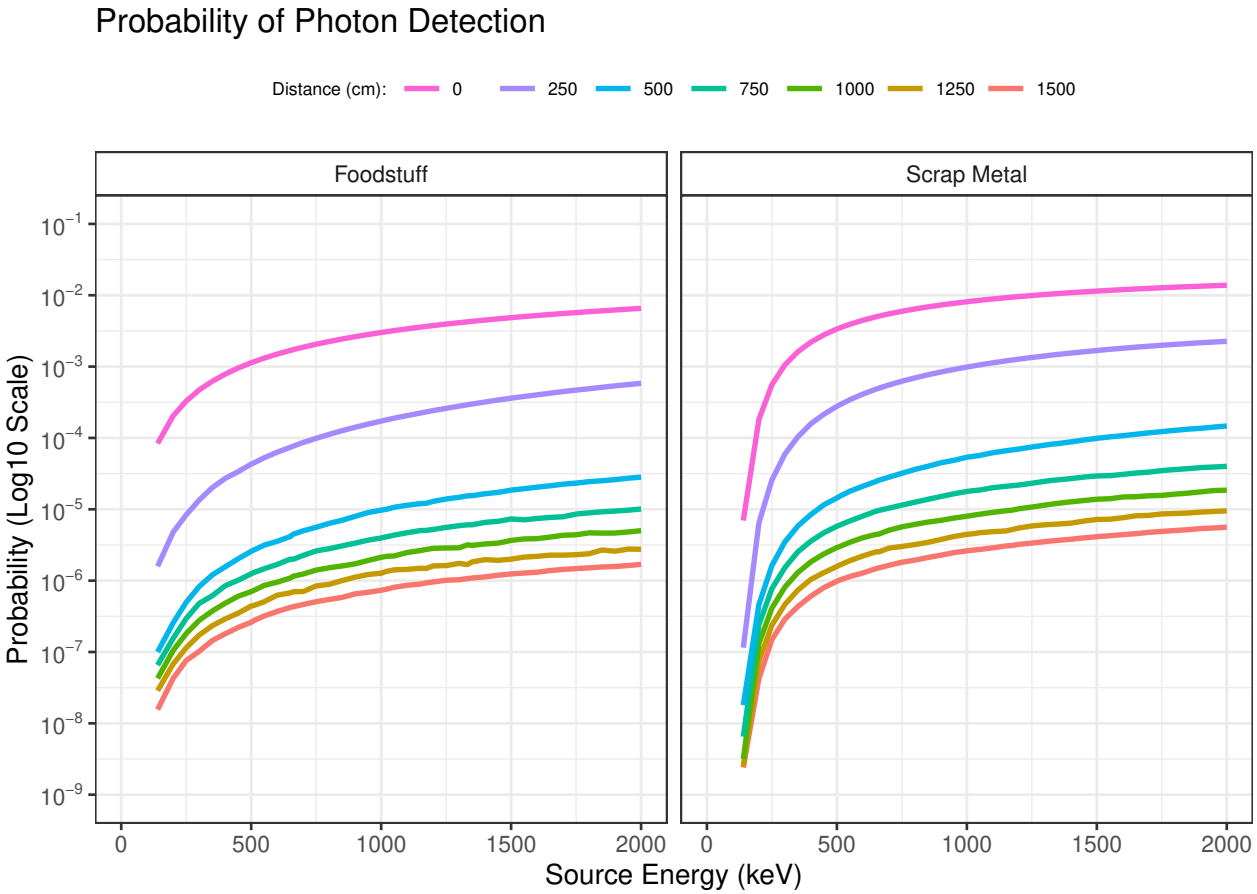

Fig. 3.5: Probability of photon detection from truck for different cargo types and distances.

This probability function is the same as the absolute efficiency function for the detectors. By integrating the absolute efficiency with the photon yield, eqn 3.5, it is possible to obtain a conversion factor from source activity to count rate on the detector. The spatial behavior of the count rate for various distances is shown in Fig. 3.6.

$$\begin{aligned} Y\left[^{137}\mathrm{Cs}; E_s\right] &= 0.851 \cdot \delta\left(E_s - 661.66\,\mathrm{keV}\right) \\ Y\left[^{60}\mathrm{Co}; E_s\right] &= 0.998 \cdot \delta\left(E_s - 1173\,\mathrm{keV}\right) + 0.999 \cdot \delta\left(E_s - 1332\,\mathrm{keV}\right) \\ Y\left[\beta^{+}; E_s\right] &= 2 \cdot \delta\left(E_s - 511\,\mathrm{keV}\right) \end{aligned} \tag{3.5}$$

These energies were all calculated exactly in MCNP, but for other photon energies, the results can be interpolated. The count rate per becquerel of activity for these sources in the two truck materials is shown in Fig. 3.6.

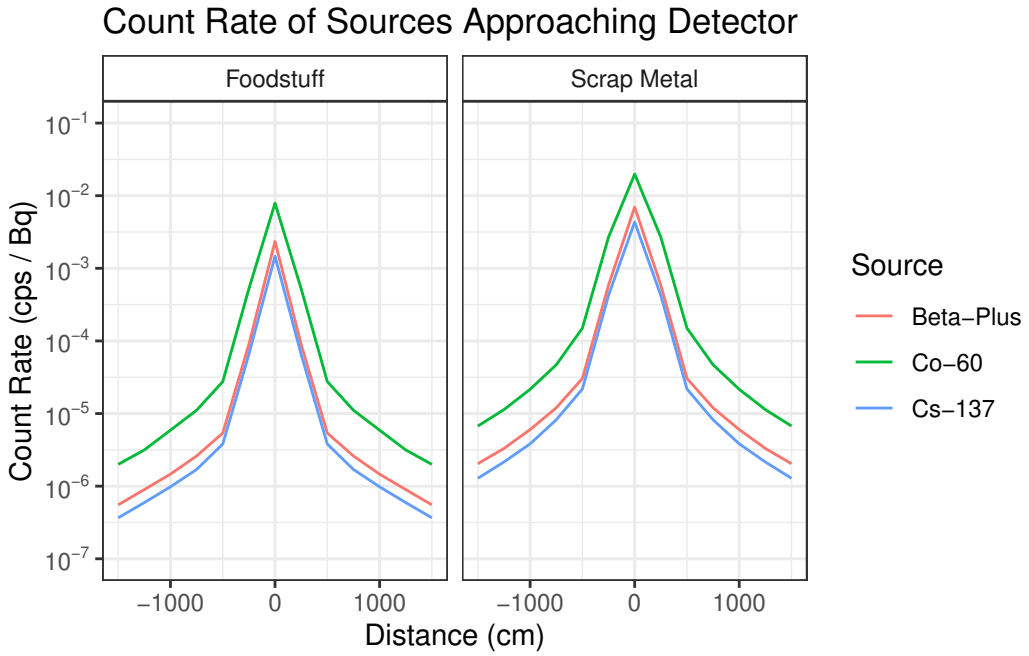

Fig. 3.6: Count rate of 1 Bq photon emitters passing through portal monitor.

All three curves show a gradual increase until the truck is within a few meters of the detectors at which point the count rate will increase rapidly. Due to the high energy of the two ^{60}Co gamma rays, the count rate per becquerel is substantially higher than compared to ^{137}Cs and beta-plus emitters. Though a beta-plus emitter has a lower energy than ^{137}Cs, there are two photons emitted per decay (through the positron-electron annihilation), leading to a higher likelihood of detection compared to the radiocesium. The photons from all three sources are more likely to be detected in the scrap metal cargo than the foodstuff cargo, as expected given their relatively high source energies.

Table 3.1: Count rate in cps (per 1Bq) of unshielded photon emitters at varying distances from portal monitor.

Contents	Position (cm)	Beta-Plus	Cs-137	Co-60
Foodstuff	0	2.34E-3	1.47E-3	7.89E-3
Foodstuff	250	8.97E-5	6.53E-5	5.23E-4
Foodstuff	500	5.39E-6	3.80E-6	2.75E-5

Contents	Position (cm)	Beta-Plus	Cs-137	Co-60
Foodstuff	750	2.60E-6	1.70E-6	1.11E-5
Foodstuff	1000	1.46E-6	9.80E-7	5.90E-6
Foodstuff	1250	8.98E-7	5.94E-7	3.16E-6
Foodstuff	1500	5.53E-7	3.66E-7	2.00E-6
Scrap Metal	0	6.98E-3	4.34E-3	1.98E-2
Scrap Metal	250	5.84E-4	4.24E-4	2.69E-3
Scrap Metal	500	3.04E-5	2.18E-5	1.50E-4
Scrap Metal	750	1.20E-5	8.20E-6	4.69E-5
Scrap Metal	1000	6.01E-6	3.83E-6	2.16E-5
Scrap Metal	1250	3.31E-6	2.15E-6	1.13E-5
Scrap Metal	1500	2.04E-6	1.28E-6	6.72E-6

Chapter 4

Discussion

4.1 Intrinsic Detection Efficiency

Through the method outlined in the introduction, the intrinsic efficiency of the detector can be calculated via the F1 and F8 tallies. Due to an unusual characteristic in the behavior of the F8 tally, all data from the lowest non-zero energy bin have been removed from the calculation, Kulesza et al. (2022). The matrix procedure was used to compute the detection efficiency for all truck position data, and the special case when the truck was at its closest approach. Additionally, MCNP runs without any truck, ground, or detector supports were performed in vacuum to compute the intrinsic efficiency using an isotropic source as a point of comparison. The data for all of these runs are included in Fig. 4.1. The measured efficiency is roughly identical for both calculations with the source present in the truck. The results of the bare isotropic source follow similar characteristics, though the efficiency is somewhat larger for energies above approximately 400 keV. All three curves peak near 320 keV, and drop to a low efficiency for higher energies. We hypothesize that the discrepancy between the bare source and the source within the truck may be explained by the averaging done between the two portal monitors for the F1 and F8 tallies used to calculate the absolute efficiency and the probability of reaching the detector.

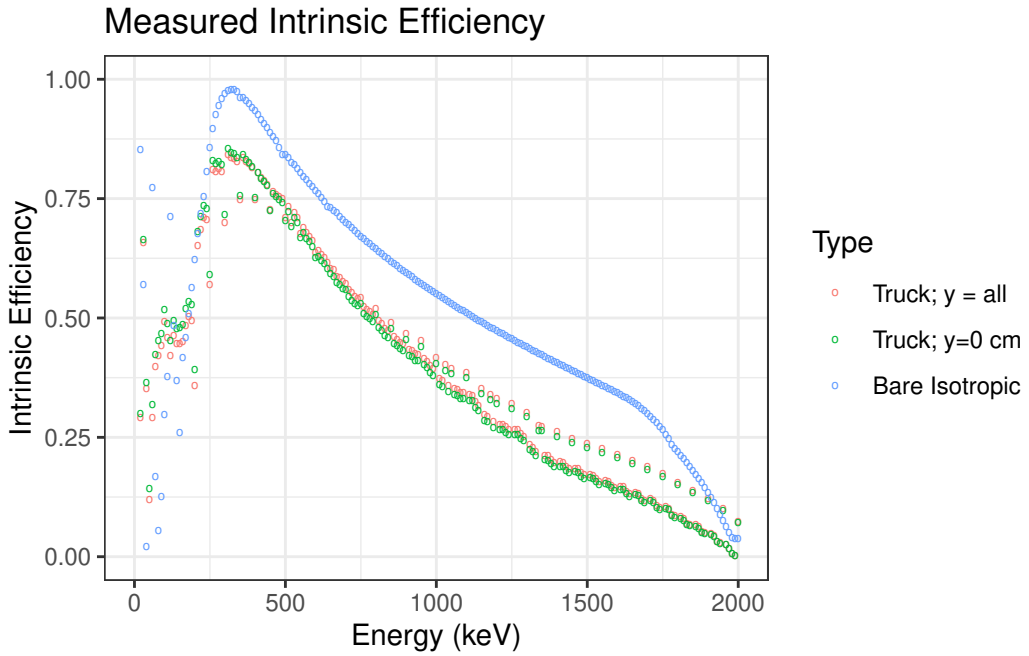

Fig. 4.1: Measured intrinsic efficiency of portal monitor. The blue circles indicate the measured efficiency using an unshielded source in a vacuum.

4.2 Absolute Detection Efficiency

Using the data for the probability of detection given emission, two different models of the absolute detection efficiency. A linear model is initially constructed due to its inferential capabilities. Due to the probability of detection spanning several decades and limitations in linear regression models, the predictive capabilities are limited to closer distances and higher energies. Therefore, this model is unable to predict the detection efficiency for nuclear materials which have low energy gamma rays with lower emission yields. That being said, there are some inferences which can be made from the model parameters. There is an indication that the absolute efficiency decreases faster than $1/\text{Distance}^4$. This likely includes both shielding effects and geometric effects. The model also indicates that, on average for the source energies considered, the detection efficiency of a truck carrying scrap metal is higher than for a truck carying foodstuff. The analytic form of the model also allows for prediction of the net counts along the different points in the truck's path, and for the time derivative

of the count rate. The time derivative of the count rate achieves a maximum and minimum when the truck's y-value is half the separation distance of the two portal monitors. This can potentially be used as an indicator for weak radiological sources which do not exceed the decision threshold.

A non-linear model is also constructed due to its ability to better predict the absolute efficiency. The non-linear model is able to better predict cross effects of different variables and fit local variations better. Future research will be done to refine the non-linear model so that it may be used in operational settings to predict the activity of different sources whose count rates are at the decision threshold. The biggest limitations in this non-linear model are due to the simplifications of the internal geometry of the truck, lack of intentional shielding which may occur for illicit sources, and low detection likelihoods for lower energy sources.

4.2.1 Linear Model of Detection Efficiency

Using the probability of detection given in eqn 3.4 and Fig. 3.5, an empirical fit can be created to predict the absolute efficiency of the detector for new source energies and positions relative to the detectors, and to infer the characteristics of the detector. The model used is given by eqn 4.1 in which $\mathrm{E} \sim \mathcal{N}\left(0, \sigma^2\right)$ represents random error of the results, and $\widehat{\beta}_i$ are estimators for model parameters. The error term contains the deviations of our observed data from the model output. The magnitude of these errors will inform the uncertainty in the model parameters. As this is an empirical fit, the equation only holds when the position is given in centimeters and the energy is given in kilo-electron-volts (denoted $\{y\}_{\mathrm{cm}}$ and $\{E_{\mathrm{s}}\}_{\mathrm{keV}}$ following ISO-IEC 80000 notation), ISO and IEC (2009). The parameter δ is used to represent whether the cargo contains scrap metal, $\delta = 1$, or whether the cargo contains foodstuff, $\delta = 0$. The base assumption is that the cargo type only has a multiplicative effect on the absolute efficiency. A logarithmic model was chosen since the probability of detection varies over several decades and can vary significantly due to small changes in the

source energy and truck position. When the truck is at its closest approach, the source is still $x_\perp = 179.5\,\text{cm}$ from the detector. This factor is included so that the model depends on the total distance from the truck to the detector.

$$\begin{aligned}
\ln\left(\varepsilon_{\text{abs}}\left(E_\text{s}, y\right)\right) &= \ln\left(\hat{\varepsilon}_{\text{abs}}\left(E_\text{s}, y\right)\right) + \text{E} \\
&= \begin{bmatrix} 1 & \delta & \ln\left(\sqrt{\{y\}_{\text{cm}}^2 + 179.5^2}\right) & \ln\left(\{E_\text{s}\}_{\text{keV}}\right) \end{bmatrix} \begin{bmatrix} \hat{\beta}_0 \\ \hat{\beta}_1 \\ \hat{\beta}_2 \\ \hat{\beta}_3 \end{bmatrix} + \text{E} \qquad (4.1) \\
\hat{\varepsilon}_{\text{abs}}\left(E_\text{s}, y\right) &= e^{\hat{\beta}_0 + \delta\hat{\beta}_1} \cdot \left(\sqrt{\{y\}_{\text{cm}}^2 + 179.5^2}\right)^{\hat{\beta}_2} \cdot \{E_\text{s}\}_{\text{keV}}^{\hat{\beta}_3}
\end{aligned}$$

The regression was performed using the `lm` function in R using weights proportional to the reciprocal of the square of the uncertainty in the logarithm of the efficiency, R Core Team (2023). The parameter values, standard uncertainties, and correlation coefficients are summarized in Table 4.1. Interestingly, the efficiency follows a $1/r^{4.031}$ curve. This likely includes the typical $1/r^2$ behavior from the isotropic emission and additional attenuation from shielding. Since the correlation coefficients are non-zero and non negligible for the off diagonal elements, the uncertainty in the logarithm of the absolute efficiency must contain additional terms to account for this, eqn 4.2. Additionally, since the logarithm of the efficiency is assumed to follow a normal distribution, the efficiency should follow a log-normal distribution. For this reason, a multiplicative uncertainty (similar to geometric standard deviation) will be used to construct confidence intervals, Turner et al. (2012).

Table 4.1: Parameter values, uncertainties, and correlation coefficients for regression model.

	Value	$u\left(\cdot\right)$	$\rho\left[\cdot, \hat{\beta}_0\right]$	$\rho\left[\cdot, \hat{\beta}_1\right]$	$\rho\left[\cdot, \hat{\beta}_2\right]$	$\rho\left[\cdot, \hat{\beta}_3\right]$
$\hat{\beta}_0$	7.084	0.165	1.000	-0.029	-0.753	-0.622
$\hat{\beta}_1$	1.002	0.013	-0.029	1.000	-0.066	0.038
$\hat{\beta}_2$	-4.031	0.025	-0.753	-0.066	1.000	-0.042

	Value	$u(\cdot)$	$\rho\left[\cdot,\hat{\beta}_0\right]$	$\rho\left[\cdot,\hat{\beta}_1\right]$	$\rho\left[\cdot,\hat{\beta}_2\right]$	$\rho\left[\cdot,\hat{\beta}_3\right]$
$\hat{\beta}_3$	1.155	0.015	-0.622	0.038	-0.042	1.000

$$
\begin{aligned}
u_{\mathrm{g}}\left(\hat{\varepsilon}_{\mathrm{abs}}\right) &= u\left(\ln\hat{\varepsilon}_{\mathrm{abs}}\right)\sqrt{\sum_{i=0}^{3}\sum_{j=0}^{3}\frac{\partial\ln\hat{\varepsilon}_{\mathrm{abs}}}{\partial\hat{\beta}_i}\frac{\partial\ln\hat{\varepsilon}_{\mathrm{abs}}}{\partial\hat{\beta}_j}\cdot\mathrm{Cov}\left[\hat{\beta}_i,\hat{\beta}_j\right]} \\
&= \sqrt{\sum_{i=0}^{3}\sum_{j=0}^{3}\frac{\partial\ln\hat{\varepsilon}_{\mathrm{abs}}}{\partial\hat{\beta}_i}\frac{\partial\ln\hat{\varepsilon}_{\mathrm{abs}}}{\partial\hat{\beta}_j}u\left(\hat{\beta}_i\right)u\left(\hat{\beta}_j\right)\cdot\rho\left[\hat{\beta}_i,\hat{\beta}_j\right]}
\end{aligned}
\tag{4.2}
$$

The assumption of utilizing a linear model (for the logarithm of the efficiency) is that the data are normally distributed, as characterized by the error term in eqn 4.1. Fig. 4.2 contains several diagnostic plots to assess this assumption. If the data were normally distributed, we would expect the relative residuals (defined as the quotient of the residual and the uncertainty in the model output) to follow a standard normal distribution. The observed distribution is skewed somewhat left, contains several local maxima, and contains more data with zero residual than would be expected. A majority of the data are still within two standard uncertainties of zero indicating this is a decent fit. The skewed behavior indicates that the model is likely to overestimate the efficiency instead of underestimate it. When the quantiles of the residuals are plotted against the quantiles of a standard normal distribution, the expected behavior is linear if the error term in the model is normally distributed. For the negative residuals, there is a significant deviation from the normal distribution, but for positive residuals and residuals near zero, there is some fit with a normal distribution. This behavior indicates the model will be inaccurate for data whose residuals are large and negative.

A of the residuals against the fitted values of the linear model is shown below, Fig. 4.2. The color of the point indicates the logarithm of the energy and the brightness indicates the logarithm of the position. The residuals which are large and negative are those at further distances and lower energies. These are data in which the probability of detection is already

low. Since the probability of detection falls off rapidly for these source configurations, it is unlikely that a log-log model would be able to capture this behavior.

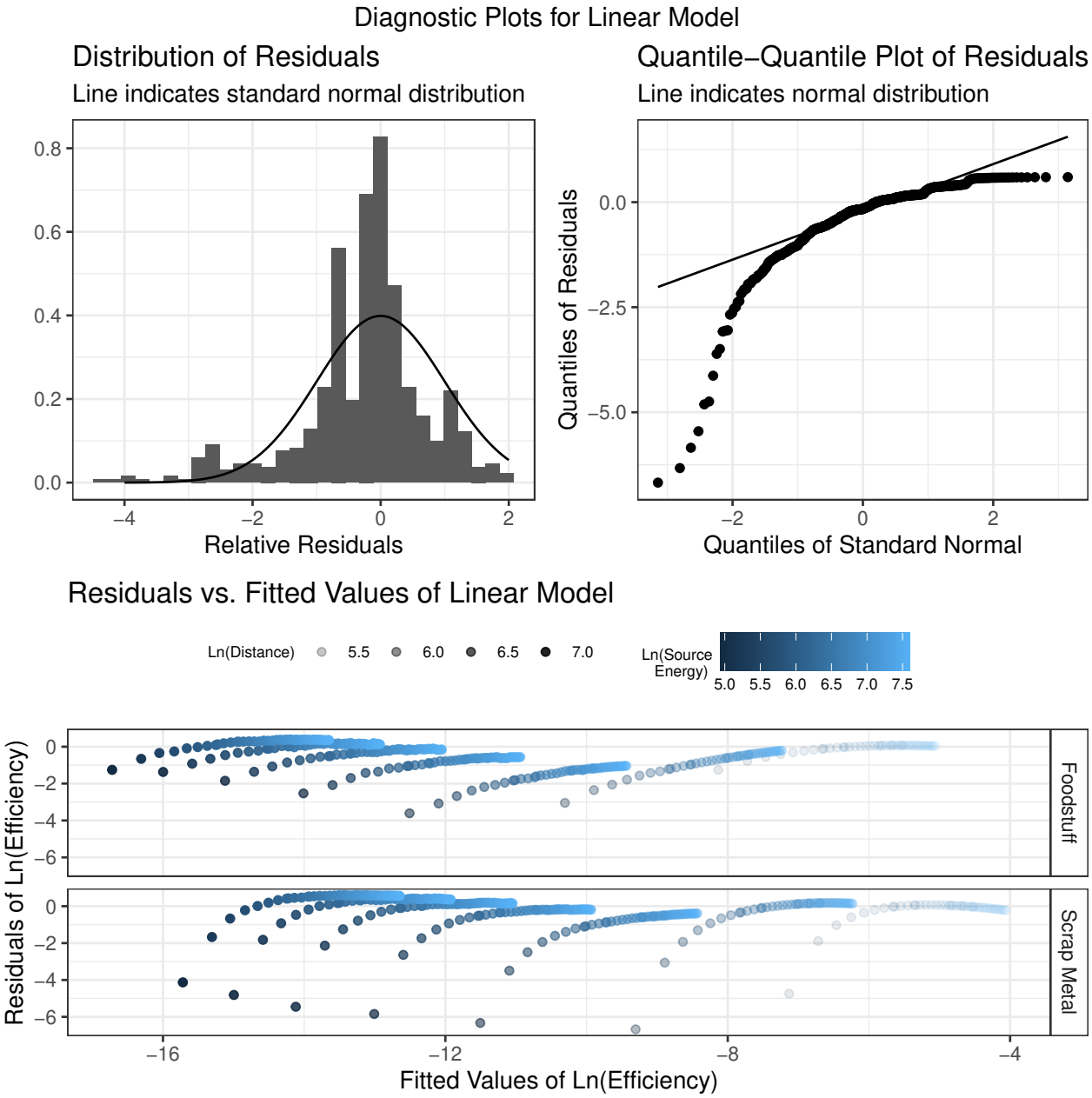

Fig. 4.2: Diagnostic plots for linear model; distribution of residuals (left), quantile-quantile plot of residuals (right), and residuals vs. fitted values (bottom).

A comparison of the linear model output and MCNP data for the absolute detection efficiency is shown in Fig. 4.3. The model does perform well for distances within about

300 cm of the source, and for energies above 500 keV. The model seems to underestimate the probability of detection for cargo containing foodstuff and seems to overestimate the probability of detection for cargo containing scrap metal.

Within the region that the model does perform well, Fig. 4.4 shows a contour plot of the efficiency. This figure can be used to make general predictions of the probability of detection for sources at different regions given expected source energies and cargo.

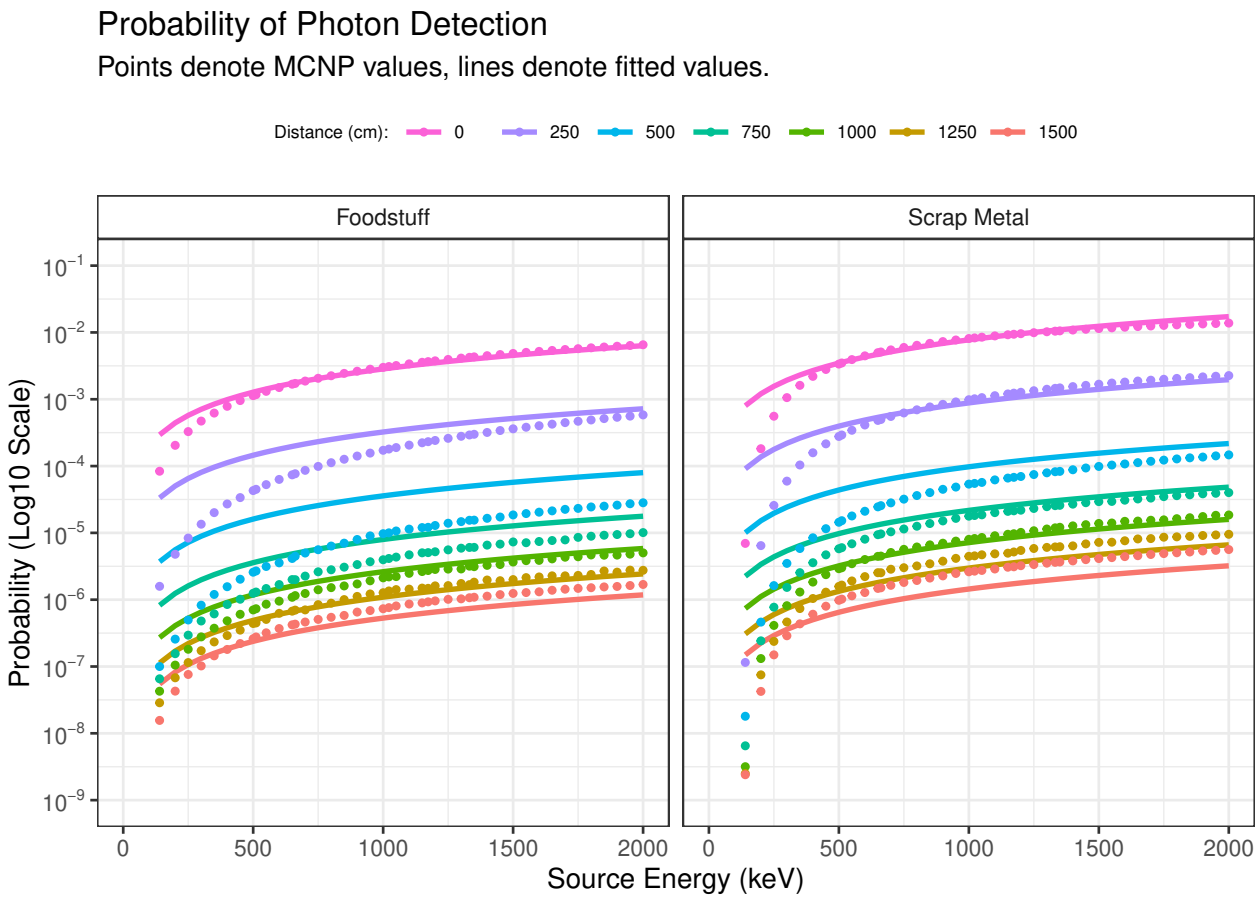

Fig. 4.3: Comparison of linear model efficiency values and MCNP values.

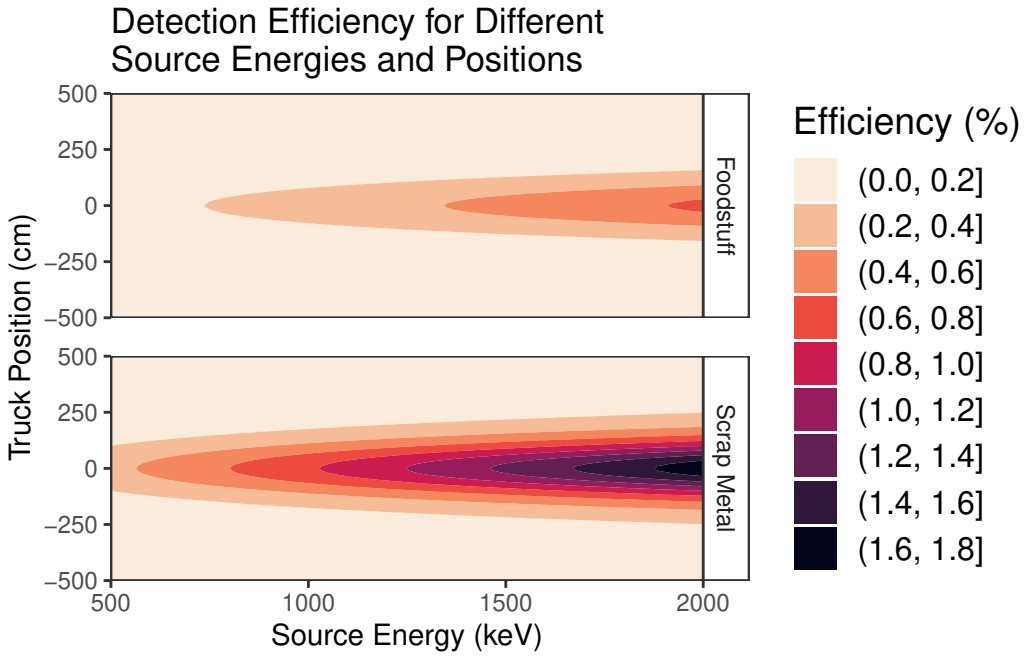

Fig. 4.4: Contour plot of detection efficiency as obtained by linear model.

Using the parameters from the linear fit, the count rate for a source with photon yield $Y(E_\mathrm{s})$ at some position y on approach can be written analytically, eqn 4.3, in which $x_\perp = 179.5$. The integral over the source energy is complicated for most continuous emission spectra, but for most radiological sources of concern, the emission spectra are a sum of Dirac-delta functions. With an analytic expression for the count rate of a source at some distance, quantities such as the rate of change of the count rate and net counts over a distance can be predicted.

$$\begin{aligned}\hat{r}_\mathrm{n}(y) &= A\int_0^\infty \hat{\varepsilon}_\mathrm{abs}(E_\mathrm{s}, y)\, Y(E_\mathrm{s})\, \mathrm{d}E_\mathrm{s} \\ &= Ae^{\hat{\beta}_0+\delta\hat{\beta}_1}\cdot\left(\{y\}_\mathrm{cm}^2 + \{x_\perp\}_\mathrm{cm}^2\right)^{\hat{\beta}_2/2}\cdot\int_0^\infty \{E_\mathrm{s}\}_\mathrm{keV}^{\hat{\beta}_3}\cdot Y\left(\{E_\mathrm{s}\}_\mathrm{keV}\right)\mathrm{d}\{E_\mathrm{s}\}_\mathrm{keV}\end{aligned} \tag{4.3}$$

The net counts between two positions y_1 and y_2 can be calculated by integrating the net count rate along the path with those endpoints. If the truck is moving with constant velocity, v, the integral over time can be replaced with an integral over position, eqn 4.4. The

net counts between two positions can be expressed in terms of the hypergeometric function, eqn 4.5, and was evaluated using the Sympy computer algebra system, Python Software Foundation (2021), Meurer et al. (2017).

$$\begin{aligned}
\hat{n}_n\left(y_1, y_2\right) &= \int_{f^{-1}(y_1)}^{f^{-1}(y_2)} \hat{r}_n\left(f(t)\right) \mathrm{d}t \\
&= \frac{1}{v} \int_{y_1}^{y_2} \hat{r}_n(z) \mathrm{d}z \\
&= \frac{A \cdot e^{\hat{\beta}_0 + g\hat{\beta}_1}}{v} \cdot \int_0^{\infty} \left\{E_\mathrm{s}\right\}_{\mathrm{keV}}^{\hat{\beta}_3} \cdot Y\left(\left\{E_\mathrm{s}\right\}_{\mathrm{keV}}\right) d\left\{E_\mathrm{s}\right\}_{\mathrm{keV}} \\
&\quad \times \int_{y_1}^{y_2} \left(y^2 + y_\perp^2\right)^{\hat{\beta}_2/2} dy \\
&= \frac{A \cdot e^{\hat{\beta}_0 + g\hat{\beta}_1}}{v} \cdot \int_0^{\infty} \left\{E_\mathrm{s}\right\}_{\mathrm{keV}}^{\hat{\beta}_3} \cdot Y\left(\left\{E_\mathrm{s}\right\}_{\mathrm{keV}}\right) \mathrm{d}\left\{E_\mathrm{s}\right\}_{\mathrm{keV}} \\
&\quad \times \left[y_2 \cdot {}_2F_1\left(\frac{1}{2}, -\frac{\hat{\beta}_2}{2}; \frac{3}{2}; -\frac{y_2^2}{y_\perp^2}\right) - y_1 \cdot {}_2F_1\left(\frac{1}{2}, -\frac{\hat{\beta}_2}{2}; \frac{3}{2}; -\frac{y_1^2}{y_\perp^2}\right) \right]
\end{aligned} \tag{4.4}$$

The hypergeometric function can be expressed in terms of the permutation and gamma functions, eqn 4.5, and has been numerically evaluated when needed, Gogolin (2014), Hankin (2016).

$$\begin{aligned}
{}_2F_1\left(a, b; c; x\right) &= \sum_{n=0}^{\infty} \frac{P\left(a, n\right) P\left(b, n\right)}{P\left(c, n\right)} \frac{x^n}{n!} \\
P\left(u, v\right) &= \frac{\Gamma\left(u+1\right)}{\Gamma\left(u-v+1\right)}
\end{aligned} \tag{4.5}$$

Using the analytic expression for net counts between two positions, we can obtain the predicted cumulative net counts along the trucks trajectory, Fig. 4.5. The linear model suggests that the maximum net counts is no achieved until the truck has gotten 2.5 m from the portal monitors.

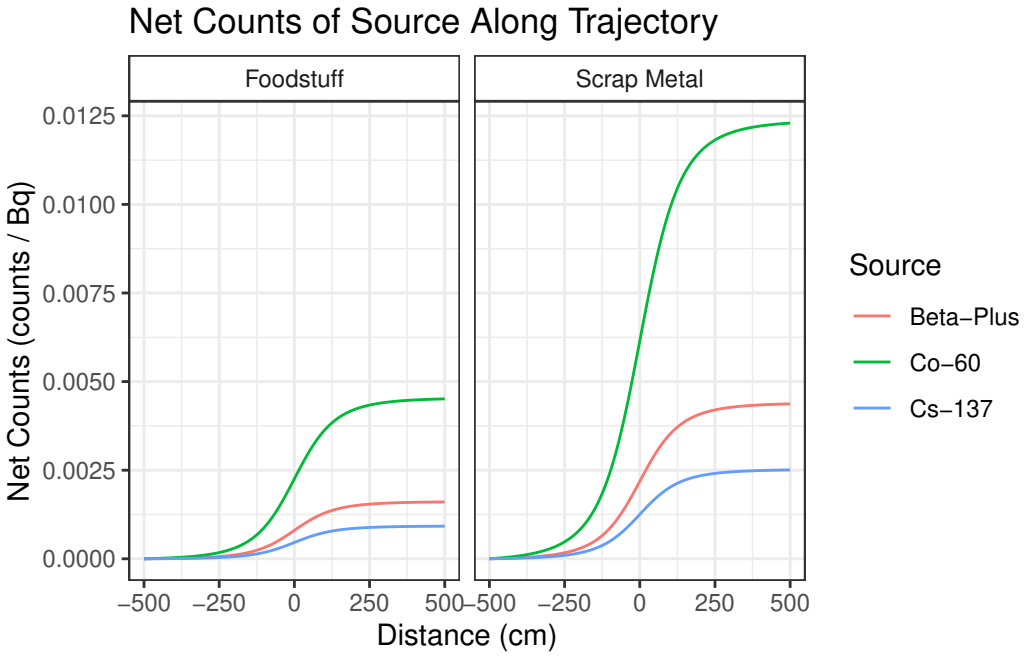

Fig. 4.5: Cumulative net counts (per decay) of common photon emitters.

The analytic expression can also be used to obtain the time derivative of the count rate. For weak radiological sources, this can be an indicator of source presence even when the net counts do not exceed the decision threshold. For a truck moving with constant velocity, the rate of change in the count rate is given by eqn 4.6. The count rate derivative reaches a maximum when the truck is at $y = -179.5\,\text{cm}$ and at a local minimum when $y = 179.5\,\text{cm}$. These correspond to half the distance between the pair of portal monitors. By measuring the count rate shortly before and after these positions, it may be possible to detect weaker sources which may not exceed the decision threshold.

$$\begin{aligned}\frac{\mathrm{d}\hat{r}_n}{\mathrm{d}t} &= \frac{\mathrm{d}y}{\mathrm{d}t}\frac{\mathrm{d}\hat{r}_n}{\mathrm{d}y} \\ &= \{y\}_{\text{cm}}\,\{v\}_{\text{cm/s}}\,\hat{\beta}_2 A e^{\hat{\beta}_0+\delta\hat{\beta}_1}\cdot\left(\{y\}_{\text{cm}}^2+\{x\}_{\perp}^2\right)^{\frac{\hat{\beta}_2}{2}-1}\cdot\int_0^{\infty}\{E_\text{s}\}_{\text{keV}}^{\hat{\beta}_3}\cdot Y\left(\{E_\text{s}\}_{\text{keV}}\right)\mathrm{d}\,\{E_\text{s}\}_{\text{keV}}\end{aligned} \tag{4.6}$$

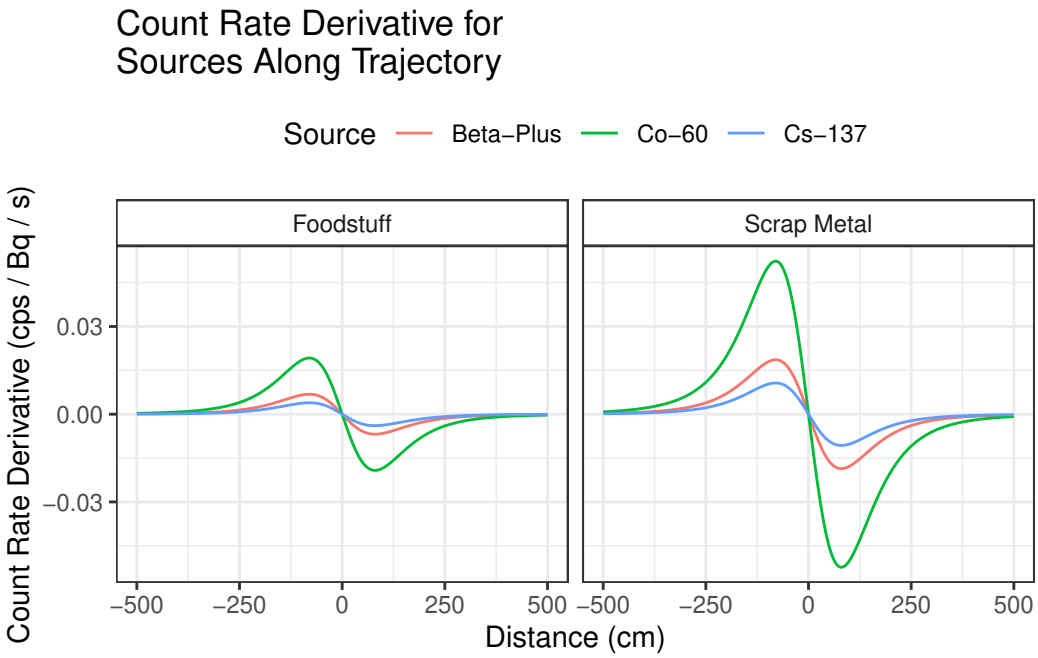

Fig. 4.6: Derivative of net count rate (per decay) of common photon emitters.

4.2.2 Multivariate Adaptive Regression Spline Model of Detection Efficiency

The primary benefit of the linear regression model is its inferential capabilities. Through an analytic expression for the detection efficiency, it is possible to analyze model parameters for how different source and truck configurations affect the detection efficiency. The analytic form can be used to predict quantities such as derivatives and integrals of the detection efficiency. The major weakness is its limited predictive capabilities. For lower energy sources and truck positions further from the detector, the model fails to predict the detection efficiency. This is compounded by the fact that the quantity of interest (detection efficiency) is the exponential of the model output.

Other regression models, such as spline fits, have far better predictive capabilities. This is due to their complicated, piecewise, non-linear functional dependence on the predictor variables which allows them to fit the data better. This functional behavior does not allow for simple analytic expressions and likely will not have many inferential capabilities. In spite

of this, a multivariate adaptive regression spline (MARS) model was developed in addition to the linear model to make better predictions. The MARS model uses a series of hinge and rectified-linear functions of the predictor variables to generate an output. Initially this will over-fit the model to the data for many hinge functions. The points which connect the functions are known as *knots*. The model then selectively removes knots and refits the data until a balance between model simplicity and accuracy is reached.

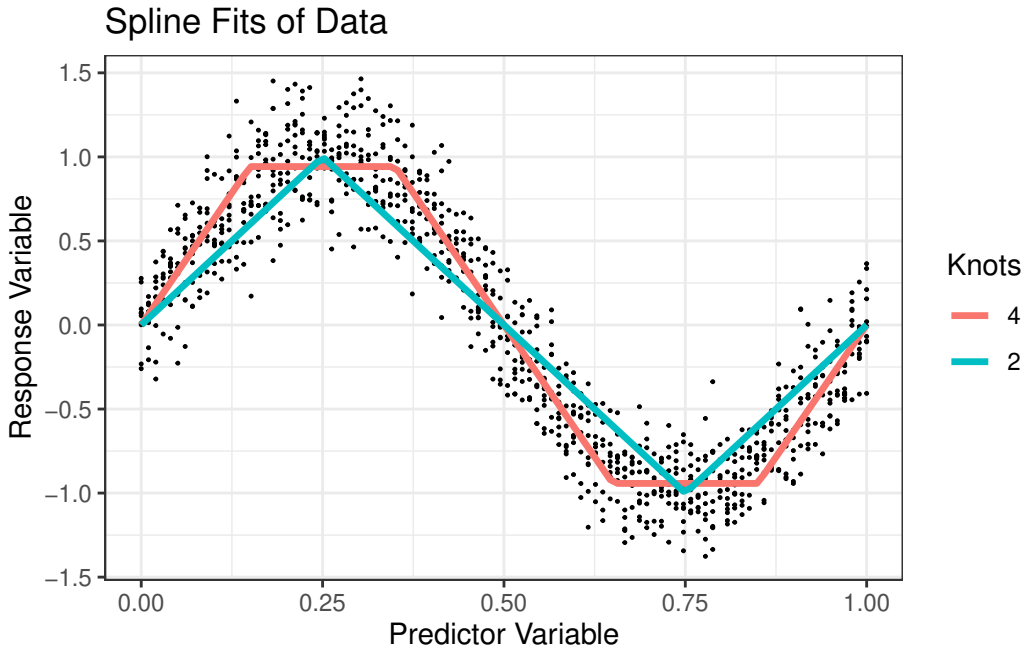

Fig. 4.7: Visualization of knot reduction in multivariate adaptive regression spline models.

The regression model was originally developed by Friedman in 1991 and has been implemented in many different software packages, Friedman (1991). The R package `earth` has been used to generate a better predictive model of the detection efficiency, Milborrow. Derived from mda:mars by T. Hastie and R. Tibshirani. (2011). Fig. 4.8 contains several diagnostic plots of the new model which fits the (natural) logarithm of the detection efficiency. Like the linear model, the MARS model assumes that the residuals follow a normal distribution. The distribution of the relative residuals shows that the values are centered around zero, with slightly more values at this point. The distribution is also slightly skewed left,

though not as significantly as the linear model. This can also be seen in the quantile-quantile plot of the residuals which show there are several large negative residuals. For regions in which the model does fit well, we can expect the normality assumption to fit well.

A plot of the residuals against the fitted values of the MARS model is shown below, Fig. 4.8. The color of the points indicates the energy and the brightness indicates the position. The residuals which are large and negative are those at further distances and lower energies. Interestingly, this model seems to perform poorly for higher energies, unlike the linear model.

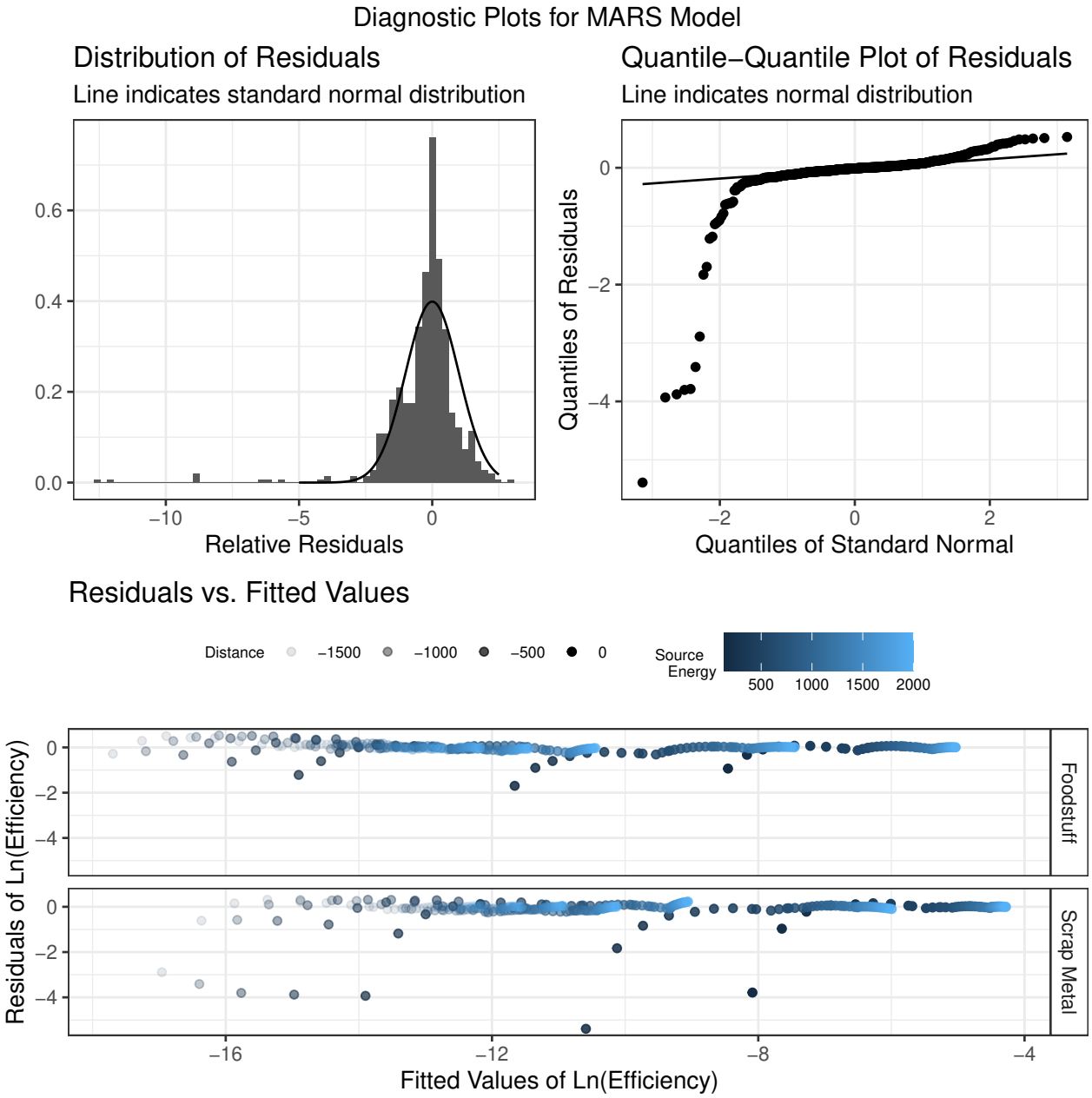

Fig. 4.8: Diagnostic plots for MARS; distribution of residuals (left), quantile-quantile plot of residuals (right), and residuals vs. fitted values (bottom).

A comparison of the MARS model output and MCNP data for the absolute detection efficiency is shown in Fig. 4.9. The model does perform well for distances within about 300 cm of the source, and for energies above 500 keV. The model seems to underestimate

the probability of detection for cargo containing foodstuff and seems to overestimate the probability of detection for cargo containing scrap metal.

Within the region that the model does perform well, Fig. 4.10 shows a contour plot of the efficiency. This figure can be used to make general predictions of the probability of detection for sources at different regions given expected source energies and cargo.

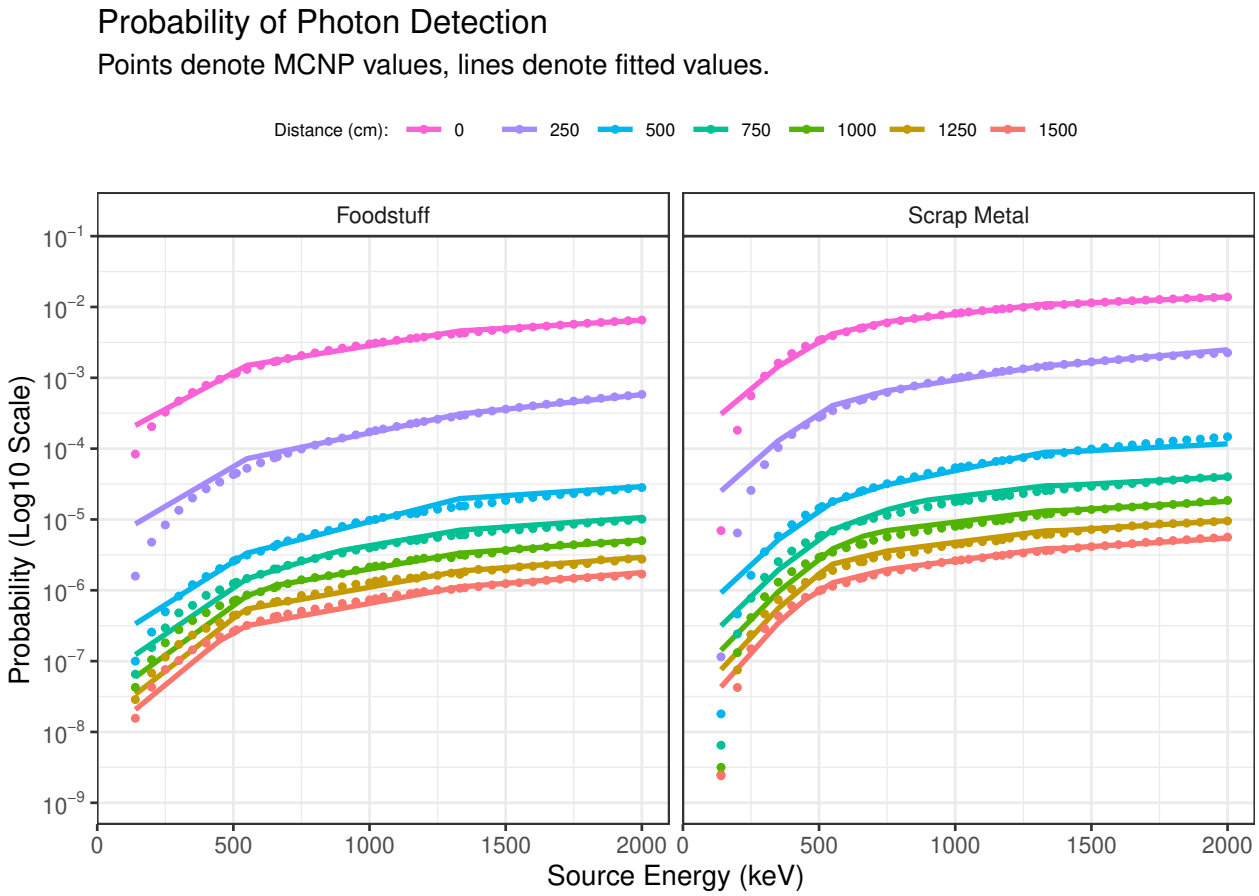

Fig. 4.9: Comparison of MARS model efficiency values and MCNP values.

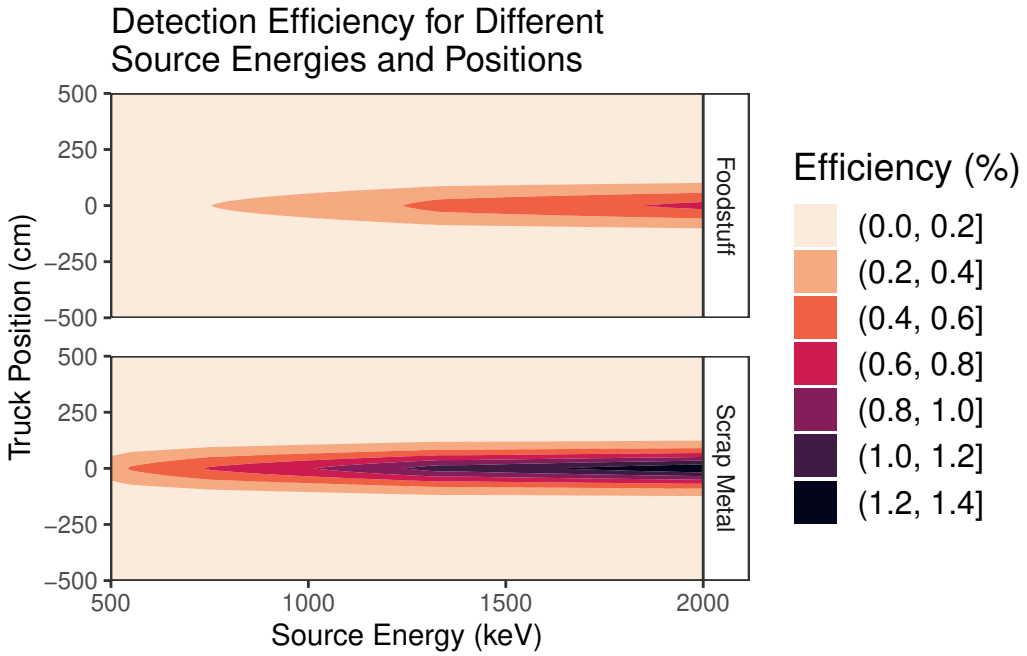

Fig. 4.10: Contour plot of detection efficiency as obtained by MARS model.

Unlike the linear regression model, there is not a clean analytic expression for the net count rate using the MARS model. If the emission spectrum of a source is discrete or can be expressed as a histogram, the count rate can be estimated using a sum over the yield and efficiency at each photon energy. The count rate at different positions for ^{137}Cs, ^{60}Co, and for a positron emitter is shown in Fig. 4.11.

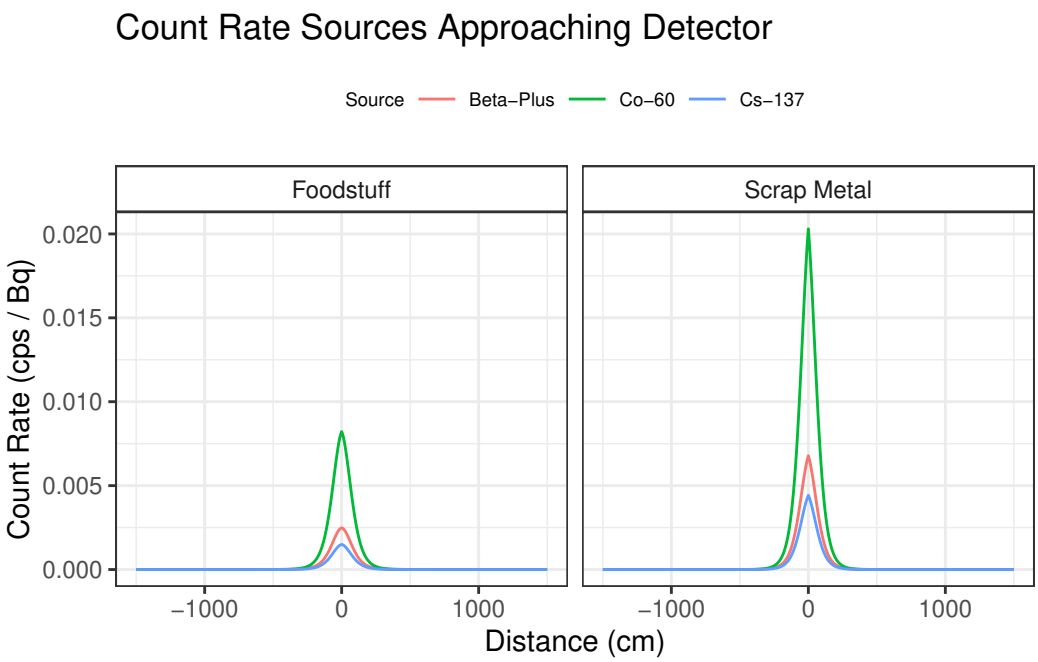

Fig. 4.11: Count rate for 1 Bq photon emitters using MARS model.

It is possible to numerically integrate and differentiate these count rates to provide estimates for these quantities. However, these estimates likely will not be as accurate or insightful as the linear model. The primary purpose of this model is to make predictions about net count rates and detection efficiency.

Chapter 5

Conclusion

The primary results of importance are the probability of photons reaching the detector and their probability of detection. As expected, the distance of the truck from the detector is a major contributor to the likelihood of detection and reaching the portal monitor. For truck distances greater than 500 cm, the probability of detection and reaching the portal monitor is decreases rapidly for increasing distances. The energy of source photon is another major contributor for the likelihood of reaching the detector and for detection. For low energies, the likelihood of photoelectric scattering in the cargo or truck is high enough that many photons will not reach the detector. Since many nuclear materials of concern emit low energy gamma rays with low emission yields, the models developed for the detection efficiency will be unable to accurately predict their measured count rates. As the initial energy increases, the probability of reaching the detector appears to asymptotically approach a fixed value for a particular position and cargo type. Once the photons have sufficient energy to reliably exit the truck, the primary factor affecting reaching the detector is whether their path will intersect with the portal monitor. Finally, there are notably differences between the foodstuff cargo and the scrap-metal cargo due to their different attenuation coefficients at different energies. For higher energy photons, the differences between the two cargo types may be an artifact of the 50% packing efficiency used for the foodstuff cargo. Under scenarios in which less foodstuff is being transported, the attenuation coefficient may be higher in scap metal for all energies.

Using the data for the probability of detection given emission, two different models of the absolute detection efficiency. A linear model is initially constructed due to its inferential capabilities. Due to the probability of detection spanning several decades and limitations in linear regression models, the predictive capabilities are limited to closer distances and higher energies. That being said, there are some inferences which can be made from the

model parameters. There is an indication that the absolute efficiency decreases faster than $1/\text{Distance}^4$. This likely includes both shielding effects and geometric effects. The model also indicates that, on average, the detection efficiency of a truck carrying scrap metal is higher than for a truck carrying foodstuff. The analytic form of the model also allows for prediction of the net counts along the different points in the truck's path, and for the time derivative of the count rate. The time derivative of the count rate achieves a maximum and minimum when the truck's y-value is half the separation distance of the two portal monitors. This can potentially be used as an indicator for weak radiological sources which do not exceed the decision threshold.

A non-linear model is also constructed due to its ability to better predict the absolute efficiency. The non-linear model is able to better predict cross effects of different variables and fit local variations better. Future research will be done to refine the non-linear model so that it may be used in operation settings to predict the activity of different sources whose count rates are at the decision threshold. These models and data can be used to make predictions of detector efficiency and net count rate detection of polyvinyl toluene photon detectors. These can be used to estimate correction factors used in ISO 11929 methodology of determining decision thresholds at portal monitoring stations. Additionally, the insights provided by the linear model can be used to identify other indicators of weaker radiological sources.

There are several variables missing from the current calculations of the detection efficiency. For thinner detectors, higher energy photons are more likely to pass through without interacting which can pose issues for thinner plastic scintillators. Sources which are intentionally shielded for illicit purposes will have a reduction in the number of photons which will exit the truck. The photons which do exit the shield may have undergone Compton scatter and will have a lower energy as they travel through the cargo and truck exterior. These effects can be incorporated by using the transmittance spectrum of photons exiting the shield as the photon emission yield, though they are not directly included in the model.

There are currently plans to perform additional MCNP calculations with varying detector thickness and shielded sources. This model only considers two cargo types with no variation in packing efficiency or mixed cargo types. The interior of these trucks also does not contain any internal structures which may be more relevant to the mixed cargo types. In the future, it may be of interest to include these in the MCNP model to ensure the model is applicable for more users.

This model also only considers the effects on the net count rate, but does not consider the background radiation suppression which can occur when a truck passes through the monitors. Within the ISO 11929 methodology, this can artificially increase the decision threshold if not corrected for and potentially let weaker sources through. This work has been done experimentally by others, but there is an interest in incorporating these effects into our model.

There are new models which may be developed to predict the behavior of other instruments used to minimize illicit radiological sources. These include sodium iodide and high purity germanium detectors in both fixed and mobile settings. These detectors have far better energy resolution than plastic scintillators and can be used for spectroscopic analysis. Given the wide applicability of these detectors, there is a potential for modeling the multi-channel behavior and deconvoluting the measured signal to obtain emission spectra of sources. Several researchers have also applied Bayesian methods to weak radiological sources to have an updating decision threshold and to make better use of past data. These methods and the use of multi-channel detectors will be the focus of future studies.

References

Altshuler B, Pasternack B. Statistical Measures of the Lower Limit of Detection of a Radioactivity Counter: Health Physics 9:293–298; 1963.

Beck P, Schmitzer C. ITRAP - INTERNATIONAL LABORATORY AND FIELD TEST SITE EXERCISE FOR RADIATION DETECTION INSTRUMENTS AND MONITORING SYSTEMS AT BORDER CROSSINGS. 2003.

Bevelacqua JJ. Health Physics Radiation-Generative Devices, Characteristics, and Hazards. Wiley-VCH ; John Wiley [distributor]; 2016.

Borchers HW. Pracma: Practical numerical math functions. 2022.

Brooks FD. Development of organic scintillators. Nuclear Instruments and Methods 162:477–505; 1979.

Browne E, Tuli JK. Nucl. Data Sheets 108, 2173. 2006.

Browne E, Tuli JK. Nucl. Data Sheets 114, 1849. 2013.

Cacuci DG (ed). Handbook of nuclear engineering. New York ; London: Springer; 2010.

Federal Highway Administration. Comprehensive Truck Size and Weight Limits Study. U.S. Department of Transportation; Report to Congress; 2016.

Firestone RB. Table of isotopes. [1/2], update 1999. 8. ed., 1999 update New York Weinheim: Wiley; 1999.

Friedman JH. Multivariate Adaptive Regression Splines. The Annals of Statistics 19:1–67; 1991.

Gesh C, Pagh R, Rucker R, Iii RW, Willaims RG iii. Compendium of Material Composition Data for Radiation Transport Modeling. Richland, Washington, US: Pacific Northwest National Laboratory; 15870-01; 2011.

Gogolin AO. Lectures on Complex Integration. Tsitsishvili EG and Komnik A, eds. Cham: Springer International Publishing; 2014.

Hankin RKS. Hypergeo: The gauss hypergeometric function. 2016.

IAEA. The Radiological Accident in Goiânia. The Radiological Accident in Goiânia. International Atomic Energy Agency; 1988.

IAEA (ed). Safety of radiation sources and security of radioactive materials: Proceedings of an International Conference on the Safety of Radiation Sources and the Security of Radioactive Materials. Vienna: International Atomic Energy Agency; 1999.

ICRP. Basic anatomical and physiological data for use in radiological protection: Reference values. Valentin J, ed. Oxford: Pergamon Press; 2003.

ICRU. ICRU Report 85: Fundamental Quantities and Units for Ionizing Radiation. Journal of the ICRU 11:NP.2–NP; 2011.

ISO. Determination of the characteristic limits (decision threshold, detection limit and limits of the confidence interval) for measurements of ionizing radiation Fundamentals and application. 2010.

ISO, IEC. Quantities and Units. 2009.

Johnson TE. Introduction to health physics. Fifth edition New York: McGraw-Hill Education; 2017.

Johnson TE, Birky BK. Health physics and radiological health. 4th ed Philadelphia: Wolters Kluwer health - Lippincott Williams & Wilkins; 2012.

Kalos MH, Whitlock PA. Monte Carlo methods. 2., revised and enlarged ed Weinheim: WILEY-VCH; 2008.

Knoll GF. Radiation detection and measurement. 4th ed Hoboken, N.J: John Wiley; 2010.

Kulesza J, Adams T, Armstrong J, Bolding S, Brown F, Bull J, Burke T, Clark A, Forster Iii R, Giron J, Grieve T, Josey C, Martz R, McKinney G, Pearson E, Rising M, Solomon Jr. C, Swaminarayan S, Trahan T, Wilson S, Zukaitis A. MCNP® Code Version 6.3.0 Theory & User Manual. LA-UR-22-30006, 1889957; 2022.

Lloyd A. Currie. Limits for Qualitative Detection and Quantitative Determination. Analytical Chemistry 40:586–593; 1968.

Lo Presti CA, Weier DR, Kouzes RT, Schweppe JE. Baseline suppression of vehicle portal monitor gamma count profiles: A characterization study. Nuclear Instruments and Methods in Physics Research Section A: Accelerators, Spectrometers, Detectors and Associated Equipment 562:281–297; 2006.

Ludlum Measurements Inc. Ludlem model 4525-series data sheet. Ludlum Measurements, Inc.; Data Sheet Model 4525 Series; 2023.

Ludlum Measurements, Inc. Ludlem model 4525 series installation guide. Ludlum Meaesurements, Inc.; Installation Guide Model 4525 Series; 2022.

Meurer A, Smith CP, Paprocki M, Čertík O, Kirpichev SB, Rocklin M, Kumar A, Ivanov S, Moore JK, Singh S, Rathnayake T, Vig S, Granger BE, Muller RP, Bonazzi F, Gupta H, Vats S, Johansson F, Pedregosa F, Curry MJ, Terrel AR, Roučka Š, Saboo A, Fernando I, Kulal S, Cimrman R, Scopatz A. SymPy: Symbolic computing in Python. PeerJ Computer Science 3:e103; 2017.

Milborrow. Derived from mda:mars by T. Hastie and R. Tibshirani. S. Earth: Multivariate adaptive regression splines. 2011.

NCRP (ed). Ionizing radiation exposure of the population of the United States: Recommendations of the National Council on Radiation Protection and Measurements. Bethesda, Md: National Council on Radiation Protection and Measurements; 2009.

NCRP (ed). Responding to a radiological or nuclear terrorism incident: A guide for decision makers ; recommendations of the National Council on Radiation Protection and Measurements. Bethesda, Md: Nat. Council on Radiation Protection and Measurements; 2010.

Oehlschlägel J, Silvestri L. Bit64: A S3 class for vectors of 64bit integers. 2020.

Panganiban HP, Kim W-C, Chung T-J, Jang G-W. Optimization of flatbed trailer frame using the ground beam structure approach. Journal of Mechanical Science and Technology 30:2083–2091; 2016.

Patriarca M, Barlow N, Cross A, Hill S, Robson A, Taylor A, Tyson J. Atomic spectrometry update: Review of advances in the analysis of clinical and biological materials, foods and beverages. Journal of Analytical Atomic Spectrometry 36:452–511; 2021.

Python Software Foundation. Python Language. 2021.

R Core Team. R: A Language and Environment for Statistical Computing. Vienna, Austria: R Foundation for Statistical Computing; 2023.

Rakes, Kelly D. Evaluating The Response Of Polyvinyl Toluene Scintillators Used In Portal Detectors. 2008.

Strick Trailers. Strick Elevator. Specification Sheet EVR-PS 12/21; 2021.

Turner JE. Atoms, radiation, and radiation protection. 3rd completely rev. and enl. ed Weinheim: Wiley-VCH; 2007.

Turner JE, Downing DJ, Bogard JS. Statistical methods in radiation physics. Weinheim, Germany: Wiley-VCH; 2012.

Wang, Zhu, Moga, Hu, Zhang. A Holistic Packaging Efficiency Evaluation Method for Loss Prevention in Fresh Vegetable cold chain. Sustainability 11:3874; 2019.

Wickham H, Averick M, Bryan J, Chang W, McGowan L, François R, Grolemund G, Hayes A, Henry L, Hester J, Kuhn M, Pedersen T, Miller E, Bache S, Müller K, Ooms J, Robinson D, Seidel D, Spinu V, Takahashi K, Vaughan D, Wilke C, Woo K, Yutani H. Welcome to the tidyverse. J Open Source Softw 4:1686; 2019.